Atmos. Chem. Phys. Discuss., doi:10.5194/acp-2015-1007, 2016
Manuscript under review for journal Atmos. Chem. Phys.
Published: 19 January 2016

Atmospheric Chemistry and Physics
Discussions

Using a combined power law and log-normal distribution model to simulate particle formation and growth in a mobile aerosol chamber

M. Olin, T. Anttila, and M. Dal Maso

Aerosol Physics Laboratory, Department of Physics, Tampere University of Technology, P.O. Box 692, 33101 Tampere, Finland

Correspondence to: M. Olin (miska.olin@tut.fi)

Abstract. We present the combined power law and log-normal distribution (PL+LN) model, a computationally efficient model to be used in simulations where the particle size distribution cannot be accurately represented by log-normal distributions, such as in simulations involving the initial steps of aerosol formation, where new particle formation and growth occur simultaneously, or in the case of inverse modelling. The model was validated against highly accurate sectional models using input parameter values that reflect conditions typical to particle formation occurring in the atmosphere and in vehicle exhaust, and tested in the simulation of a particle formation event performed in a mobile aerosol chamber at Mäkelänkatu street canyon measurement site in Helsinki, Finland. The number, surface area, and mass concentrations in the chamber simulation were conserved with the relative errors lower than 2 % using the PL+LN model, whereas a moment-based log-normal model and sectional models with the same computing time as with the PL+LN model caused relative errors up to 10 % and 135 %, respectively.

1 Introduction

Particle size distribution is the most important characteristic of aerosols, as it controls aerosol deposition to the human respiratory system and their behavior in the atmosphere. To accurately simulate aerosol evolution, the particle size distribution needs to be modelled carefully because particle size also strongly affects the rates of several aerosol processes, such as condensation, coagulation, and deposition. Aerosol models typically model one or more parameter of the size distribution, such as particle number or mass concentration of the total particle size range or of several size ranges separately.

The most accurate shape-preserving methods to model a particle size distribution are sectional methods, in which the size distribution is split into separate size sections. The accuracy of a sectional model can be controlled by the number of the size sections. Increasing the number of sections increases accuracy, but the computational cost is also increased. In multidimensional simulations, such as in Computational Fluid Dynamics (CFD) simulations, computational efficiency is a key property of the model. Simulations involving inverse modelling (Verheggen and Mozurkewich, 2006), where the values of model input parameters (e.g., new particle formation rate J or condensational growth rate $g = \frac{\mathrm{d}D_\mathrm{p}}{\mathrm{d}t}$) are varied systematically to find out the values that most exactly produce the measured results, may suffer from long computing times even in one-dimensional cases.

Sectional methods vary depending on the conserved property of the aerosol. Only a single property, e.g. particle number, particle surface area, or particle mass concentration, can be conserved in the simulation but other properties will suffer from numerical diffusion, which is seen as the overestimation of the non-conserved properties (Wu and Biswas, 1998). Less numerical diffusion can be obtained by using a moving-center fixed-sectional method, of which size sections have fixed boundaries but the centers of the sections are changed so that number and mass concentrations are conserved (Jacobson, 1997). However, implementing the moving-center fixed-sectional method in Eulerian simulation, such as in CFD simulation, with simultaneous new particle formation, condensation, coagulation, and transportation is challenging due to discontinuous behavior of the section variables (all particles of a section are transferred to an adjacent section when the center of a section exceeds a section boundary during growth), computationally time-consuming due to the transfer of the particles between the sections, and memory-consuming due to the requirement of storing the center values of the sections too. Wang and Zhang (2012) have modelled simultaneous new particle formation and growth within diesel exhaust plumes using the moving-center fixed-sectional method in three dimensional CFD simulation and have obtained promising results for particle size distributions compared to the measured distributions with only 8 size sections in a decade. However, they did not report comparison between their model and any highly accurate aerosol model; thus, the amount of numerical diffusion is unknown.

Other approaches to model the particle size distribution are methods based on the moments of the distribution (Whitby and McMurry, 1997), which are both computationally efficient (Mitrakos et al., 2007) and have continuous behavior of the variables. The number of the conserved properties of the aerosol is controlled by the number of the modelled moments; e.g. conserving number, surface area, and mass concentrations can be obtained by modelling the corresponding three moments. The number of the variables being stored during the simulation is the number of the modelled moments, which is significantly less compared to sectional methods, in which the number of the variables can be several hundreds. The major drawback in the methods based on moments is that the size distribution needs to be presented with a pre-defined function, unless the quadrature-method of moments (QMOM, McGraw (1997)) is used. QMOM provides accurate results (Barrett and Webb, 1998) but the reconstruction of the distribution parameters from the moments is not unique (Mitrakos et al., 2007). The typical choice for the size distribution function is the log-normal distribution or the combination of several log-normal distributions. They correspond well with many laboratory aerosols and aged aerosols, but during the initial steps of the formation and growth of aerosol the size distribution can differ significantly. For example, Tammet and Kulmala (2014) recommend two-power law for the size distribution of atmospheric aerosols measured at least in Northern Europe. Two-power law distribution has four parameters, which implies that four moments are required for the reconstruction of the parameters from the moments, if the distribution is modelled using the moment method. However, there is no analytical solution for the system of equations of the two-power law approach, and solving the system of equations with four variables numerically is computationally very expensive.

The general dynamic equation (GDE) for the number concentration of a size section N_j, with new particle formation rate $J(t)$ and condensational growth rate $g(t,D_\mathrm{p})$ without any other aerosol processes, is (Seinfeld and Pandis, 2006)

$$\frac{\mathrm{d}N_j}{\mathrm{d}t} = \begin{cases} J(t) - \frac{g(t,D_\mathrm{p})}{\Delta D_j} N_j, & j = 1 \\ \frac{g(t,D_\mathrm{p})}{\Delta D_j} N_{j-1} - \frac{g(t,D_\mathrm{p})}{\Delta D_j} N_j, & j > 1 \end{cases}, \tag{1}$$

where ΔD_j is the diameter width of the section j. In the case of simultaneous new particle formation and condensation with time- and size-independent rates, the analytical solution for the GDE provides the particle size distribution

$$\frac{\mathrm{d}N}{\mathrm{d}\ln D_\mathrm{p}} = \begin{cases} \frac{J}{g} D_\mathrm{p}, & D_1 \le D_\mathrm{p} \le D_2 \\ 0, & \text{otherwise} \end{cases}, \tag{2}$$

where D_1 is the diameter of the newly formed particle (assumed constant) and D_2 is the largest diameter. Equation (2) is in the form of a power law where the power of D_p is unity. In a realistic particle formation process, $J(t)$ and $g(t, D_\mathrm{p})$ do not remain constants and other aerosol processes affect also; thus, the power of D_p can differ and log-normal features will appear in the distribution. Here, we present a method to express the particle size distribution as a combination of a power law and a log-normal distribution. This moment-based combined power law and log-normal distribution model is validated against highly accurate sectional models and tested in the simulation of a particle formation event performed in a mobile aerosol chamber.

2 Model description

The combined power law (PL) and log-normal (LN) distribution model (PL+LN) is based on the sum of these distributions. The PL distribution handles the formation and the initial growth of new particles; the LN distribution represents the log-normal shape of the distribution and it is formed by coagulation and condensation from the PL distribution.

2.1 Particle size distributions

2.1.1 Power law distribution

The formulation of the PL distribution originates from Eq. (2), where the power of D_p is allowed to vary,

$$\left.\frac{\mathrm{d}N}{\mathrm{d}\ln D_\mathrm{p}}\right|_\mathrm{PL} = \begin{cases} \frac{N_\mathrm{PL}\alpha}{D_2^\alpha - D_1^\alpha} D_\mathrm{p}^\alpha, & D_1 \le D_\mathrm{p} \le D_2, \alpha \neq 0 \\ \frac{N_\mathrm{PL}}{\ln(D_2/D_1)}, & D_1 \le D_\mathrm{p} \le D_2, \alpha = 0 \\ 0, & \text{otherwise} \end{cases}, \tag{3}$$

where N_PL is the total particle number concentration, α is the slope parameter, D_1 is the smallest diameter, and D_2 is the largest diameter of the PL distribution. In this form, the PL distribution has four parameters, which leads to numerical challenges for the reconstruction of the distribution parameters from four moments. However, by fixing one parameter, only three moments are required to be modelled and the reconstruction will simplify. Here, the value of D_1 is fixed to the diameter of a newly formed particle, which is also physically sensible because that value is not expected to vary significantly; in atmospheric particle formation, the value is about $1.5 \pm 0.3\ \mathrm{nm}$ (Kulmala et al., 2013).

Three moments required in the modelling of the PL distribution with parameters N_{PL}, α, and D_2 are, in this article, number N_{PL}, surface area S_{PL}, and mass M_{PL} concentration

$$N_{\mathrm{PL}} = N_{\mathrm{PL}} \tag{4}$$

$$\begin{aligned} S_{\mathrm{PL}} &= \int_{-\infty}^{\infty} s_{\mathrm{p}} \left.\frac{\mathrm{d}N}{\mathrm{d}\ln D_{\mathrm{p}}}\right|_{\mathrm{PL}} \mathrm{d}\ln D_{\mathrm{p}} \\ &= s_1\, N_{\mathrm{PL}}\, \frac{\alpha}{\alpha+2}\, \frac{\left(\frac{D_2}{D_1}\right)^{\alpha+2} - 1}{\left(\frac{D_2}{D_1}\right)^{\alpha} - 1} \end{aligned} \tag{5}$$

$$\begin{aligned} M_{\mathrm{PL}} &= \int_{-\infty}^{\infty} m_{\mathrm{p}} \left.\frac{\mathrm{d}N}{\mathrm{d}\ln D_{\mathrm{p}}}\right|_{\mathrm{PL}} \mathrm{d}\ln D_{\mathrm{p}} \\ &= m_1\, N_{\mathrm{PL}}\, \frac{\alpha}{\alpha+3}\, \frac{\left(\frac{D_2}{D_1}\right)^{\alpha+3} - 1}{\left(\frac{D_2}{D_1}\right)^{\alpha} - 1}, \end{aligned} \tag{6}$$

where s_{p} and m_{p} are the surface area and the mass of a particle, respectively, and s_1 and m_1 are the surface area and the mass of a newly formed particle, respectively. All particles are assumed to be spherical. Equations (5) and (6) have singularities at α values of -3, -2, and 0. In those cases, the equations have different formulations, and from now on, the singularity equations are not shown here due to the fact that α will never equal a singularity value precisely in a simulation. Modelling the composition of particles can be done by separating the mass concentration to different components using the assumption that the particles are internally mixed, i.e. the composition does not vary with the particle diameter. The modelling of the particle composition is, however, outside of the scope of this article.

The reconstruction of the distribution parameters from the moments N_{PL}, S_{PL}, and M_{PL} is performed as follows. The zeroth moment N_{PL} is already one of the distribution parameters, but S_{PL} and M_{PL} are not. The latter are converted to the system of equations of two unknown variables α and $d = D_2/D_1$

$$\begin{cases} \frac{M_{\mathrm{PL}}}{N_{\mathrm{PL}}} \frac{1}{m_1} & = \left(\frac{\alpha}{\alpha+3}\right)\left(\frac{d^{\alpha+3}-1}{d^{\alpha}-1}\right) \\ \frac{M_{\mathrm{PL}}}{S_{\mathrm{PL}}} \frac{s_1}{m_1} & = \left(\frac{\alpha+2}{\alpha+3}\right)\left(\frac{d^{\alpha+3}-1}{d^{\alpha+2}-1}\right) \end{cases}. \tag{7}$$

However, there is no analytical solution for this system of equations, but solving two variables numerically is sufficiently fast for this purpose. A pre-calculated interpolation table is used in the numerical solution, with which a more rapid calculation is obtained. The interpolation table increases the memory cost of the model, but as the table is unique (independent on temporal or spatial coordinate) it needs to be stored in one memory location only.

Atmos. Chem. Phys. Discuss., doi:10.5194/acp-2015-1007, 2016
Manuscript under review for journal Atmos. Chem. Phys.
Published: 19 January 2016

2.1.2 Log-normal distribution

The LN distribution is expressed by the equation

$$\left.\frac{\mathrm{d}N}{\mathrm{d}\ln D_\mathrm{p}}\right|_\mathrm{LN} = \frac{N_\mathrm{LN}}{\sqrt{2\pi}\ln\sigma}\exp\left[-\frac{\ln^2(D_\mathrm{p}/D_\mathrm{g})}{2\ln^2\sigma}\right], \tag{8}$$

where N_LN is the total particle number concentration, σ the geometric standard deviation, and D_g the geometric mean diameter of the LN distribution. The LN distribution is also modelled as three moments N_LN, S_LN, and M_LN. Following the method of Whitby and McMurry (1997), the reconstruction of the distribution parameters from the moments can be performed using the equations

$$N_\mathrm{LN} = N_\mathrm{LN} \tag{9}$$
$$D_\mathrm{g} = 6^{-2/3}\,\pi^{-5/6}\,\rho^{2/3}\,N_\mathrm{LN}^{-5/6}\,S_\mathrm{LN}^{3/2}\,M_\mathrm{LN}^{-2/3} \tag{10}$$
$$\ln^2\sigma = \ln\left(6^{2/3}\,\pi^{1/3}\,\rho^{-2/3}\,N_\mathrm{LN}^{1/3}\,S_\mathrm{LN}^{-1}\,M_\mathrm{LN}^{2/3}\right), \tag{11}$$

where ρ is the particle density.

2.1.3 Connection between the distributions

The combined particle distribution is modelled as the superposition of the PL and the LN distributions

$$\left.\frac{\mathrm{d}N}{\mathrm{d}\ln D_\mathrm{p}}\right|_\mathrm{PL+LN} = \left.\frac{\mathrm{d}N}{\mathrm{d}\ln D_\mathrm{p}}\right|_\mathrm{PL} + \left.\frac{\mathrm{d}N}{\mathrm{d}\ln D_\mathrm{p}}\right|_\mathrm{LN}. \tag{12}$$

Figure 1 represents examples of the PL+LN distribution. PL distributions with different values of α are shown in the left pane; $N = 10^6\,\mathrm{cm^{-3}}$, $D_1 = 1.5\,\mathrm{nm}$, and $D_2 = 5\,\mathrm{nm}$ are equal in all four distributions. The right pane shows the PL distribution with values $N = 10^6\,\mathrm{cm^{-3}}$, $\alpha = 1$, $D_1 = 1.5\,\mathrm{nm}$, and $D_2 = 3\,\mathrm{nm}$, the LN distribution with values $N = 5\times10^5\,\mathrm{cm^{-3}}$, $D_\mathrm{g} = 4\,\mathrm{nm}$, and $\sigma = 1.1$, and the combination of them.

A schematic presentation of the connections between the distributions is shown in Fig. 2. Particles in the PL distribution formed by new particle formation and grown by condensation and coagulation (Fig. 3) are transferred to the LN distribution through three intermodal processes: coagulational transfer, intermodal coagulation, and condensational transfer. The coagulational transfer is accounted by intramodal coagulation, i.e. self-coagulation, which is basically an intramodal process, but in this model it is used to initiate the LN distribution by transferring the coalesced resultant particles larger than D_2 to the LN distribution. The coagulational transfer is described in more detail in Sec. 2.2.5. After the LN distribution is initiated, particles of the both distributions begin to collide intermodally (the intermodal coagulation). In that case, the resultant particles are always assigned to the LN distribution, which is thought to consist of larger particles than the PL distribution.

The intramodal coagulation of the PL distribution remains the only process initiating the formation of the LN distribution. Therefore, in the case of low particle number concentration, i.e. low intramodal coagulation rate, the formation of the LN distribution is slow; thus, the combined distribution would be mainly in a power law form. However, in realistic particle formation events, log-normal features in the size distribution are widely observed (Hinds, 1999). This is due to time- and size-dependent J, g, or particle loss rate caused by coagulation to background particles or deposition to walls. The model described here does not connect the formation of the LN distribution with the latter processes. Therefore, log-normal features can be generated artificially to the PL+LN distribution by transferring some of the particles from the PL distribution to the LN distribution. This transfer is calculated through condensation (the condensational transfer). Particles that are to be grown beyond the diameter D_2 are transferred to the LN distribution by the condensational transfer instead of keeping them in the PL distribution and increasing the value of D_2. The condensational transfer is described in more detail in Sec. 2.2.5.

2.2 Aerosol processes

The general dynamic equation for a particular moment X $(= N_{\mathrm{PL}}, S_{\mathrm{PL}}, M_{\mathrm{PL}}, N_{\mathrm{LN}}, S_{\mathrm{LN}}, \text{ or } M_{\mathrm{LN}})$ in a one-dimensional (temporal coordinate only) simulation is

$$\frac{\mathrm{d}X}{\mathrm{d}t} = \mathrm{npf}_X + \mathrm{cond}_X + \mathrm{coag}_X + \mathrm{loss}_X^{\mathrm{coag}} + \mathrm{loss}_X^{\mathrm{dep}} + \mathrm{transfer}_X^{\mathrm{coag}} + \mathrm{transfer}_X^{\mathrm{cond}}, \qquad (13)$$

of which terms denote new particle formation, condensation, coagulation, coagulational losses, depositional losses, coagulational transfer, and condensational transfer, respectively. The formulation of the terms is described next.

2.2.1 New particle formation

New particle formation is modelled by a term

$$\mathrm{npf}_X = \begin{cases} J(t), & X = N_{\mathrm{PL}} \\ J(t)\,s_1, & X = S_{\mathrm{PL}} \\ J(t)\,m_1, & X = M_{\mathrm{PL}} \\ 0, & X = N_{\mathrm{LN}}, S_{\mathrm{LN}}, \text{or } M_{\mathrm{LN}} \end{cases}, \qquad (14)$$

where $J(t)$ can be calculated, e.g., through any nucleation theory, in which $J(t)$ depend also on vapor concentrations and temperature, for example. However, finding the correct formulation for $J(t)$ is outside of the scope of this article; thus, we decided to use formation rate as an input parameter that can be either a constant (J) or a time-dependent function ($J(t)$). Additionally, inverse modelling is done to obtain $J(t)$ from measured particle number concentrations.

The sizes of a newly formed particle (D_1, s_1, and m_1) can be obtained from nucleation theories, but they are assumed to be constants here. In the case where $J(t)$ suddenly drops to zero but condensation still continues, concentration of particles with diameters around D_1 would subsequently decrease down to zero due to the growth of newly formed particles to larger diameters. Therefore, D_1, as a parameter of the PL distribution, should be a variable to model the distribution accurately. However, this would change the distribution back to a more complex four-parameter distribution that is outside of the scope of this article. In that case or with smoothly decreasing $J(t)$, α has a tendency to increase.

2.2.2 Condensation

Condensation rate $[\mathrm{kg/m^3 s}]$ of vapor v on a particle distribution i, PL or LN, can be modelled as (Olin et al., 2015)

$$\mathrm{cond}_{M_i} = \int_{-\infty}^{\infty} \frac{\mathrm{d}m_{\mathrm{p},v}}{\mathrm{d}t} \left.\frac{\mathrm{d}N}{\mathrm{d}\ln D_\mathrm{p}}\right|_i \mathrm{d}\ln D_\mathrm{p}, \tag{15}$$

where $\frac{\mathrm{d}m_{\mathrm{p},v}}{\mathrm{d}t}$ is the mass growth rate of a particle [kg/s] due to vapor v is (Lehtinen and Kulmala, 2003)

$$\frac{\mathrm{d}m_{\mathrm{p},v}}{\mathrm{d}t} = 2\pi(D_\mathrm{p}+D_v)(\mathcal{D}_\mathrm{p}+\mathcal{D}_v)(C_{v,\infty}-C_{v,\mathrm{p}})\frac{Kn+1}{0.377Kn+1+\frac{4}{3\phi}(Kn^2+Kn)}, \tag{16}$$

D_v is the diameter of a vapor molecule. $\mathcal{D}_\mathrm{p}$ and $\mathcal{D}_v$ are the diffusion coefficients of a particle and of a vapor molecule, respectively. $C_{v,\infty}$ and $C_{v,\mathrm{p}}$ are concentration of the vapor in the far-field and over the particle surface, respectively. ϕ and Kn are the mass accommodation coefficient and the Knudsen number, respectively. The concentration $C_{v,\mathrm{p}}$ is

$$C_{v,\mathrm{p}} = \Gamma_v\, C_{v,\mathrm{sat}} \exp\left(\frac{4\mathcal{S}m_v}{k_\mathrm{B}T\rho D_\mathrm{p}}\right), \tag{17}$$

where Γ_v, $C_{v,\mathrm{sat}}$, and m_v are activity, the saturation concentration, and the molecule mass of the vapor, respectively, $\mathcal{S}$ is surface tension, k_B is the Boltzmann constant, and T is temperature.

In one-dimensional simulation, the mass growth rate can be considered a function of time and the particle diameter

$$\frac{\mathrm{d}m_{\mathrm{p},v}}{\mathrm{d}t} = \frac{\mathrm{d}m_{\mathrm{p},v}}{\mathrm{d}t}(t, D_\mathrm{p}) \tag{18}$$

if the other parameters in Eq. (16) are considered also. Here, the mass growth rate (single-component case) is expressed using condensational growth rate $g(t, D_\mathrm{p})$

$$\frac{\mathrm{d}m_\mathrm{p}}{\mathrm{d}t}(t, D_\mathrm{p}) = \frac{\mathrm{d}m_\mathrm{p}}{\mathrm{d}D_\mathrm{p}} \cdot \frac{\mathrm{d}D_\mathrm{p}}{\mathrm{d}t}(t, D_\mathrm{p}) = \frac{\pi}{2}\rho D_\mathrm{p}^2 g(t, D_\mathrm{p}). \tag{19}$$

Hence, the condensation rate for a particle distribution becomes

$$\mathrm{cond}_{M_i} = \frac{\pi}{2}\rho \int_{-\infty}^{\infty} D_\mathrm{p}^2 g(t, D_\mathrm{p}) \left.\frac{\mathrm{d}N}{\mathrm{d}\ln D_\mathrm{p}}\right|_i \mathrm{d}\ln D_\mathrm{p}, \tag{20}$$

which has an analytical solution for both distributions when $g(t, D_\mathrm{p})$ can be expressed with a polynomial of D_p. The mass growth rate is proportional to D_p^2 if the following conditions are met: 1) the particle size is in free-molecular regime, 2) $D_p \gg D_v$, 3) $C_{v,\infty} \gg C_{v,\mathrm{p}}$. The latter one applies when the particle size is large or when the vapor has low saturation vapor pressure. Since particle sizes near the molecular size are modelled in this article, only the first condition applies satisfactorily. However, for the sake of convenience, the mass growth rate is assumed to be proportional to D_p^2. As for new particle formation rate $J(t)$, the main point in this article is not to provide the correct formulation for $g(t, D_\mathrm{p})$, but to compare different models, and additionally to perform inverse modelling to obtain $g(t)$ from the time evolution of measured aerosol size distributions. Due to the assumption of the proportionality of the mass growth rate, the condensational growth rate becomes size-independent, and finally, the condensation terms used in Eq. (13) become

$$\mathrm{cond}_X = \begin{cases} 0, & X = N_i \\ 2\pi\, g(t) \int_{-\infty}^{\infty} D_\mathrm{p}\, \mathrm{d}N_i, & X = S_i \\ \frac{\pi}{2} \rho\, g(t) \int_{-\infty}^{\infty} D_\mathrm{p}^2\, \mathrm{d}N_i, & X = M_i \end{cases} \tag{21}$$

where $\mathrm{d}N_i$ is an abbreviation of

$$\left.\frac{\mathrm{d}N}{\mathrm{d}\ln D_\mathrm{p}}\right|_i \mathrm{d}\ln D_\mathrm{p}. \tag{22}$$

The analytical solutions for Eqs. (21) are

$$\mathrm{cond}_X = X\, g(t) \cdot \begin{cases} 0, & X = N_\mathrm{PL} \\ \frac{2}{D_1}\left(\frac{\alpha+2}{\alpha+1}\right)\left(\frac{d^{\alpha+1}-1}{d^{\alpha+2}-1}\right), & X = S_\mathrm{PL} \\ \frac{3}{D_1}\left(\frac{\alpha+3}{\alpha+2}\right)\left(\frac{d^{\alpha+2}-1}{d^{\alpha+3}-1}\right), & X = M_\mathrm{PL} \\ 0, & X = N_\mathrm{LN} \\ \frac{2}{D_\mathrm{g}} \exp\left(-\frac{3}{2}\ln^2\sigma\right), & X = S_\mathrm{LN} \\ \frac{3}{D_\mathrm{g}} \exp\left(-\frac{5}{2}\ln^2\sigma\right), & X = M_\mathrm{LN} \end{cases} \tag{23}$$

when α is not -3, -2, or -1.

2.2.3 Coagulation

Coagulation is modelled as intramodal coagulation within the PL distribution and within the LN distribution, and as intermodal coagulation from the PL distribution to the LN distribution. The coagulation terms derived from the equations of Whitby and

McMurry (1997) are

$$\begin{aligned}\mathrm{coag}_{N_{\mathrm{PL}}} = &-\frac{1}{2}\int\limits_{-\infty}^{\infty}\int\limits_{-\infty}^{\infty}\beta(D_\mathrm{p},D'_\mathrm{p})\,\mathrm{d}N_\mathrm{PL}\,\mathrm{d}N'_\mathrm{PL}\\ &-\int\limits_{-\infty}^{\infty}\int\limits_{-\infty}^{\infty}\beta(D_\mathrm{p},D'_\mathrm{p})\,\mathrm{d}N_\mathrm{PL}\,\mathrm{d}N'_\mathrm{LN}\end{aligned}\tag{24}$$

$$\begin{aligned}\mathrm{coag}_{S_{\mathrm{PL}}} = &-\frac{1}{2}\int\limits_{-\infty}^{\infty}\int\limits_{-\infty}^{\infty}\left[2s_\mathrm{p}-\left(s_\mathrm{p}^{\frac{3}{2}}+s_\mathrm{p}'^{\frac{3}{2}}\right)^{\frac{2}{3}}\right]\beta(D_\mathrm{p},D'_\mathrm{p})\,\mathrm{d}N_\mathrm{PL}\,\mathrm{d}N'_\mathrm{PL}\\ &-\int\limits_{-\infty}^{\infty}\int\limits_{-\infty}^{\infty}s_\mathrm{p}\,\beta(D_\mathrm{p},D'_\mathrm{p})\,\mathrm{d}N_\mathrm{PL}\,\mathrm{d}N'_\mathrm{LN}\end{aligned}\tag{25}$$

$$\mathrm{coag}_{M_{\mathrm{PL}}} = -\int\limits_{-\infty}^{\infty}\int\limits_{-\infty}^{\infty}m_\mathrm{p}\,\beta(D_\mathrm{p},D'_\mathrm{p})\,\mathrm{d}N_\mathrm{PL}\,\mathrm{d}N'_\mathrm{LN}\tag{26}$$

$$\mathrm{coag}_{N_{\mathrm{LN}}} = -\frac{1}{2}\int\limits_{-\infty}^{\infty}\int\limits_{-\infty}^{\infty}\beta(D_\mathrm{p},D'_\mathrm{p})\,\mathrm{d}N_\mathrm{LN}\,\mathrm{d}N'_\mathrm{LN}\tag{27}$$

$$\begin{aligned}\mathrm{coag}_{S_{\mathrm{LN}}} = &-\frac{1}{2}\int\limits_{-\infty}^{\infty}\int\limits_{-\infty}^{\infty}\left[2s_\mathrm{p}-\left(s_\mathrm{p}^{\frac{3}{2}}+s_\mathrm{p}'^{\frac{3}{2}}\right)^{\frac{2}{3}}\right]\beta(D_\mathrm{p},D'_\mathrm{p})\,\mathrm{d}N_\mathrm{LN}\,\mathrm{d}N'_\mathrm{LN}\\ &+\int\limits_{-\infty}^{\infty}\int\limits_{-\infty}^{\infty}\left[\left(s_\mathrm{p}^{\frac{3}{2}}+s_\mathrm{p}'^{\frac{3}{2}}\right)^{\frac{2}{3}}-s'_\mathrm{p}\right]\beta(D_\mathrm{p},D'_\mathrm{p})\,\mathrm{d}N_\mathrm{PL}\,\mathrm{d}N'_\mathrm{LN}\end{aligned}\tag{28}$$

$$\mathrm{coag}_{M_{\mathrm{LN}}} = \int\limits_{-\infty}^{\infty}\int\limits_{-\infty}^{\infty}m_\mathrm{p}\,\beta(D_\mathrm{p},D'_\mathrm{p})\,\mathrm{d}N_\mathrm{PL}\,\mathrm{d}N'_\mathrm{LN},\tag{29}$$

where $\beta(D_\mathrm{p},D'_\mathrm{p})$ is the coagulation coefficient of particles with diameters D_p and D'_p calculated with the equation

$$\beta(D_\mathrm{p},D'_\mathrm{p}) = 2\pi(D_\mathrm{p}+D'_\mathrm{p})(\mathcal{D}_\mathrm{p}+\mathcal{D}'_\mathrm{p})f(Kn_\mathrm{coag}),\tag{30}$$

where $f(Kn_\mathrm{coag})$ is the transition regime function of Dahneke (1983)

$$f(Kn_\mathrm{coag}) = \frac{1+Kn_\mathrm{coag}}{1+2Kn_\mathrm{coag}+2Kn_\mathrm{coag}^2},\tag{31}$$

where Kn_coag is the Knudsen number for coagulation

$$Kn_\mathrm{coag} = \frac{4(\mathcal{D}_\mathrm{p}+\mathcal{D}'_\mathrm{p})}{(D_\mathrm{p}+D'_\mathrm{p})\sqrt{\bar{c}^2+\bar{c}'^2}},\tag{32}$$

where $\bar{c}$ and $\bar{c}'$ are the mean thermal velocities of particles with the diameters of D_p and D'_p.

The integrals in Eqs. (24) – (29) cannot be solved analytically in the transition regime because Eq. (31) cannot be presented in a polynomial form. Therefore, the integrals are calculated numerically. Gaussian quadratures are used here to reduce the associated computing time; they provide the optimal particle diameters and their weights for efficient evaluation of the integrals. The Hermite-Gauss quadrature (Steen et al., 1969) is used in the integrals involving the LN distribution, as the density function of the LN distribution Eq. (8) is in the form of the weight function of the Hermite-Gauss quadrature e^{-x^2}. E.g., an integral

$$\int\limits_{-\infty}^{\infty} \beta(D_\mathrm{p}, D'_\mathrm{p}) \left.\frac{\mathrm{d}N}{\mathrm{d}\ln D_\mathrm{p}}\right|_\mathrm{LN} \mathrm{d}\ln D_\mathrm{p} \tag{33}$$

$$= \frac{N_\mathrm{LN}}{\sqrt{2\pi}\ln\sigma} \int\limits_{-\infty}^{\infty} \beta(D_\mathrm{p}, D'_\mathrm{p}) \exp\left[-\frac{\ln^2(D_\mathrm{p}/D_\mathrm{g})}{2\ln^2\sigma}\right] \mathrm{d}\ln D_\mathrm{p}$$

becomes, using the Hermite-Gauss quadrature,

$$\frac{N_\mathrm{LN}}{\sqrt{\pi}} \sum_{j=1}^{n} w_j \beta(D_j, D'_\mathrm{p}) \tag{34}$$

where D_j and w_j are the abscissa and the weight for the bin j obtained from the quadrature, and n is the degree of the quadrature. In this article, the degree of $n = 5$ is used for the LN distribution denoting that the integrals are calculated with five diameter values. The integrals involved in the PL distribution are in the form of D_p^α which is not a weight function of any specific quadrature; therefore, a Gaussian quadrature for this purpose was developed. E.g., an integral

$$\int\limits_{\ln D_1}^{\ln D_2} \beta(D_\mathrm{p}, D'_\mathrm{p}) \left.\frac{\mathrm{d}N}{\mathrm{d}\ln D_\mathrm{p}}\right|_\mathrm{PL} \mathrm{d}\ln D_\mathrm{p}$$

$$= \frac{N_\mathrm{PL}\alpha}{D_2^\alpha - D_1^\alpha} \int\limits_{\ln D_1}^{\ln D_2} \beta(D_\mathrm{p}, D'_\mathrm{p}) D_\mathrm{p}^\alpha \,\mathrm{d}\ln D_\mathrm{p} \tag{35}$$

becomes, using the quadrature developed here,

$$\frac{N_\mathrm{PL}\ln d^\alpha}{d^\alpha - 1} \sum_{j=1}^{n} w_j \beta(D_j, D'_\mathrm{p}) \tag{36}$$

where D_j and w_j are the abscissa and the weight for the bin j obtained from the quadrature. The degree of $n = 4$ is used for the PL distribution.

The degrees of the quadratures, 4 and 5, are relatively low, which reduces the accuracy of the coagulation modelling, but due to double integrals in the coagulation terms, the computations for the coagulation coefficient is performed n squared (here $4 \times 4 = 16$, $4 \times 5 = 20$, or $5 \times 5 = 25$) times. Therefore, the degrees are kept low to maintain computational efficiency.

2.2.4 Particle losses

The losses due to coagulation of the particles in the PL+LN distribution to the background distribution not included in the PL+LN distribution are considered the coagulational losses. Particles in the background distribution are assumed to be significantly larger than the particles in the PL+LN distribution. Therefore, the particle diameters of the background distribution can be approximated with a single diameter value, e.g., $\mathrm{CMD_{bg}}$ (count median diameter). According to Kerminen and Kulmala (2002), the coagulation coefficient will then become

$$\beta(D_\mathrm{p}, \mathrm{CMD_{bg}}) \approx \beta(D_1, \mathrm{CMD_{bg}}) \left(\frac{D_\mathrm{p}}{D_1}\right)^{l_\mathrm{bg}}, \tag{37}$$

where l_bg is the exponent depending on $\mathrm{CMD_{bg}}$. The value of l_bg ranges between -2 and -1 (Lehtinen et al., 2007). The coagulational loss term, e.g., for a number concentration is

$$\mathrm{loss}_{N_i}^{\mathrm{coag}} = N_\mathrm{bg} \int\limits_{-\infty}^{\infty} \beta(D_\mathrm{p}, \mathrm{CMD_{bg}}) \mathrm{d}N_i \approx N_\mathrm{bg} \beta(D_1, \mathrm{CMD_{bg}}) D_1^{-l_\mathrm{bg}} \int\limits_{-\infty}^{\infty} D_\mathrm{p}^{l_\mathrm{bg}} \mathrm{d}N_i, \tag{38}$$

in which the last integral can be solved analytically. The analytical solutions for the coagulational loss terms are

$$\mathrm{loss}_X^{\mathrm{coag}} = X N_\mathrm{bg} \cdot \begin{cases} \beta(D_1, \mathrm{CMD_{bg}}) \left(\frac{\alpha}{\alpha + l_\mathrm{bg}}\right) \left(\frac{d^{\alpha + l_\mathrm{bg}} - 1}{d^{\alpha} - 1}\right), & X = N_\mathrm{PL} \\ \beta(D_1, \mathrm{CMD_{bg}}) \left(\frac{\alpha + 2}{\alpha + 2 + l_\mathrm{bg}}\right) \left(\frac{d^{\alpha + 2 + l_\mathrm{bg}} - 1}{d^{\alpha + 2} - 1}\right), & X = S_\mathrm{PL} \\ \beta(D_1, \mathrm{CMD_{bg}}) \left(\frac{\alpha + 3}{\alpha + 3 + l_\mathrm{bg}}\right) \left(\frac{d^{\alpha + 3 + l_\mathrm{bg}} - 1}{d^{\alpha + 3} - 1}\right), & X = M_\mathrm{PL} \\ \beta(D_\mathrm{g}, \mathrm{CMD_{bg}}) \exp\left[\frac{1}{2} l_\mathrm{bg}^2 \ln^2 \sigma\right], & X = N_\mathrm{LN} \\ \beta(D_\mathrm{g}, \mathrm{CMD_{bg}}) \exp\left[\left(\frac{1}{2} l_\mathrm{bg}^2 + 2 l_\mathrm{bg}\right) \ln^2 \sigma\right], & X = S_\mathrm{LN} \\ \beta(D_\mathrm{g}, \mathrm{CMD_{bg}}) \exp\left[\left(\frac{1}{2} l_\mathrm{bg}^2 + 3 l_\mathrm{bg}\right) \ln^2 \sigma\right], & X = M_\mathrm{LN} \end{cases} \tag{39}$$

when α is not 0 or $-l_\mathrm{bg}$.

The losses to walls due to diffusion of particles are considered the depositional losses. They are modelled with the method of Hussein et al. (2009), in which the deposition rate of particles in a test chamber is

$$\lambda = \frac{1}{V} \sum_w A_w u \tag{40}$$

where V is the volume of the chamber, A_w is the surface area of the wall w, and u is the deposition velocity of particles. A simple approximation for the deposition velocity is used here

$$u \propto D_\mathrm{p}^{-1}, \tag{41}$$

which is valid for particles smaller than $100\,\mathrm{nm}$ according to Lai and Nazaroff (2000). The depositional loss term, e.g, for a number concentration now become

$$\mathrm{loss}_{N_i}^{\mathrm{dep}} = \int\limits_{-\infty}^{\infty} \lambda \mathrm{d}N_i = k_\mathrm{dep} \int\limits_{-\infty}^{\infty} D_\mathrm{p}^{-1} \mathrm{d}N_i \tag{42}$$

where all effects, except the effect of the diameter, are included in the deposition coefficient k_{dep}. The last integral can be solved analytically, from which the depositional loss terms become

$$\text{loss}_X^{\text{dep}} = X k_{\text{dep}} \cdot \begin{cases} D_1^{-1}\left(\frac{\alpha}{\alpha-1}\right)\left(\frac{d^{\alpha-1}-1}{d^{\alpha}-1}\right), & X = N_{\text{PL}} \\ D_1^{-1}\left(\frac{\alpha+2}{\alpha+1}\right)\left(\frac{d^{\alpha+1}-1}{d^{\alpha+2}-1}\right), & X = S_{\text{PL}} \\ D_1^{-1}\left(\frac{\alpha+3}{\alpha+2}\right)\left(\frac{d^{\alpha+2}-1}{d^{\alpha+3}-1}\right), & X = M_{\text{PL}} \\ D_{\text{g}}^{-1}\exp\left(\frac{1}{2}\ln^2\sigma\right), & X = N_{\text{LN}} \\ D_{\text{g}}^{-1}\exp\left(-\frac{3}{2}\ln^2\sigma\right), & X = S_{\text{LN}} \\ D_{\text{g}}^{-1}\exp\left(-\frac{5}{2}\ln^2\sigma\right), & X = M_{\text{LN}} \end{cases} \tag{43}$$

when α is not 0 or 1.

The effect of particle losses on the PL distribution is seen as decreased α. In the trivial case, as in Eq. (1), α becomes less than zero when $k_{\text{dep}} > g$. This effect is due to increased losses with increasing particle diameters because larger particles have longer residence times from the moment since their formation. However, Eq. (41) counteracts in this effect by decreasing the deposition velocity with increasing particle size, but with small g, the effect of increased residence time dominates over the the effect of decreased deposition velocity. Additionally, the coagulational losses further decrease α.

2.2.5 Intermodal particle transfer

The intermodal coagulation is included together with the intramodal coagulation in the coagulation terms (coag_X) seen in Eqs. (24) – (29). The coagulational ($\text{transfer}_X^{\text{coag}}$) and condensational ($\text{transfer}_X^{\text{cond}}$) transfer are modelled as follows.

Particles with the diameter higher than the cut diameter

$$D_{\text{coag}} = \left(D_2^3 - D_{\text{p}}'^3\right)^{1/3} \tag{44}$$

form particles with the diameter higher than D_2 after coagulating with a particle having a diameter of D_{p}', assuming full coalescence (Fig. 2). Those resultant particles are transferred from the PL distribution to the LN distribution, because their particle diameters will correspond with the form of a log-normal distribution rather than a power law distribution, which can be observed using a highly accurate sectional model. The coagulational transfer terms are negative for the PL distribution and positive for the LN distribution to conserve the moments, and they are expressed as

$$\mathrm{transfer}_{N_\mathrm{PL}} = -\,\mathrm{transfer}_{N_\mathrm{LN}} = -\frac{1}{2}\int\limits_{-\infty}^{\infty}\int\limits_{\ln D_\mathrm{coag}}^{\infty} \beta(D_\mathrm{p}, D_\mathrm{p}')\,\mathrm{d}N_\mathrm{PL}\,\mathrm{d}N_\mathrm{PL}' \tag{45}$$

$$\mathrm{transfer}_{S_\mathrm{PL}} = -\,\mathrm{transfer}_{S_\mathrm{LN}} = -\frac{1}{2}\int\limits_{-\infty}^{\infty}\int\limits_{\ln D_\mathrm{coag}}^{\infty} \left(s_\mathrm{p}^{\frac{3}{2}} + s_\mathrm{p}'^{\frac{3}{2}}\right)^{\frac{2}{3}} \beta(D_\mathrm{p}, D_\mathrm{p}')\,\mathrm{d}N_\mathrm{PL}\,\mathrm{d}N_\mathrm{PL}' \tag{46}$$

$$\mathrm{transfer}_{M_\mathrm{PL}} = -\,\mathrm{transfer}_{M_\mathrm{LN}} = -\frac{1}{2}\int\limits_{-\infty}^{\infty}\int\limits_{\ln D_\mathrm{coag}}^{\infty} \left(m_\mathrm{p} + m_\mathrm{p}'\right) \beta(D_\mathrm{p}, D_\mathrm{p}')\,\mathrm{d}N_\mathrm{PL}\,\mathrm{d}N_\mathrm{PL}', \tag{47}$$

which are calculated using the quadrature technique as in the case of the coagulation terms.

Considering a time step of Δt in a Lagrangian simulation, particles larger than $D_\mathrm{cond} = D_2 - g\,\Delta t$ will grow due to condensation to become larger than D_2 (Fig. 2). Modelling condensation only, the value of D_2 at the next time step would increase to $D_2 + g\,\Delta t$. The condensational transfer is used to transfer the particles in the PL distribution with the diameters of $D_\mathrm{cond} < D_\mathrm{p} < D_2$ to the LN distribution. However, if the condensational transfer is modelled fully, D_2 would never increase and all condensation would affect the LN distribution only. In that case, the distributions would separate from each other. For this reason, the effect of condensational transfer is dampened using a factor γ as a multiplier in the condensational transfer equations. The factor can obtain values between 0 and 1, and it describes how the particles are distributed between the PL and the LN distributions. The number of particles in the PL distribution to be transferred to the LN distribution due to the condensational transfer in the time step of Δt is

$$N_{\mathrm{PL}\to\mathrm{LN}} = \gamma \int\limits_{\ln D_\mathrm{cond}}^{\ln D_2} \left.\frac{\mathrm{d}N}{\mathrm{d}\ln D_\mathrm{p}}\right|_\mathrm{PL} \mathrm{d}\ln D_\mathrm{p}. \tag{48}$$

Considering infinitesimally small time step $\Delta t \to 0$, D_cond approaches D_2 and $N_{\mathrm{PL}\to\mathrm{LN}}$ approaches

$$\gamma \frac{g\Delta t}{D_2} \left.\frac{\mathrm{d}N}{\mathrm{d}\ln D_\mathrm{p}}\right|_{\mathrm{PL},\, D_\mathrm{p}=D_2}. \tag{49}$$

The transferred amounts for S and M are obtained in the same approach as in Eq. (21), and they are negative for the PL distribution and positive for the LN distribution. Hence, the term for the condensational transfer becomes

$$\mathrm{transfer}_X^\mathrm{cond} = \gamma \frac{g(t)}{D_2} \left.\frac{\mathrm{d}N}{\mathrm{d}\ln D_\mathrm{p}}\right|_{\mathrm{PL},\, D_\mathrm{p}=D_2} \cdot \begin{cases} -1, & X = N_\mathrm{PL} \\ -s_2, & X = S_\mathrm{PL} \\ -m_2, & X = M_\mathrm{PL} \\ +1, & X = N_\mathrm{LN} \\ +s_2, & X = S_\mathrm{LN} \\ +m_2, & X = M_\mathrm{LN} \end{cases}, \tag{50}$$

Atmos. Chem. Phys. Discuss., doi:10.5194/acp-2015-1007, 2016
Manuscript under review for journal Atmos. Chem. Phys.
Published: 19 January 2016

where s_2 and m_2 are the surface area and the mass of the particle with the diameter of D_2. Condensational transfer does not alter the moments of the total distribution, it only transfers the particles between the distributions; therefore, the value of γ has a minor effect only on the moments, but a noticeable effect on the shape of the PL+LN distribution.

3 Model validation and test simulations

The PL+LN model was validated and tested with simulations of artificial test cases and a real particle formation case. The validation was done against sectional models that yield accurate results due to a large number of size sections. Two types of sectional models were used: fixed-sectional (FS) and moving-center fixed-sectional (MC) models. The FS model provides the best accuracy for the particle number concentration and the MC model for the mass concentration, when a high number of size sections is modelled. The results from different models and from measurement data are examined by comparing the relative errors of the moments (N, S, and M) and the variables GMD (geometric mean diameter) and GSD (geometric standard deviation). GMD and GSD can be calculated from a continuous or from a discrete total distribution with the equations

$$\ln \mathrm{GMD} = \frac{1}{N}\int_{-\infty}^{\infty} \ln D_\mathrm{p}\,\mathrm{d}N = \frac{1}{N}\sum_j N_j \ln D_{\mathrm{p},j} \tag{51}$$

$$\ln^2 \mathrm{GSD} = \frac{1}{N}\int_{-\infty}^{\infty} \ln^2\left(\frac{D_\mathrm{p}}{\mathrm{GMD}}\right)\mathrm{d}N = \frac{1}{N}\sum_j N_j \ln^2\left(\frac{D_{\mathrm{p},j}}{\mathrm{GMD}}\right), \tag{52}$$

where $D_{\mathrm{p},j}$ is the particle diameter in the center of the size section j. The reference models, with which the relative errors are calculated, are FS models, with the exception of the mass moment M for which the reference model is the MC model.

The diameter of a newly formed particle was assumed to be a constant, $D_1 = 1.6\,\mathrm{nm}$, in all cases. The value was chosen because it is in the range of a relevant size of a particle from which atmospheric aerosol formation starts (Kulmala et al., 2007) and of a size of a smallest particle that can be detected with the Particle Size Magnifier (PSM) with the detection efficiency of nearly unity (Vanhanen et al., 2011). Single-component modelling was performed assuming a mixture with the particle bulk density of $\rho = 1.4\,\mathrm{g/cm^3}$ as the component. The value was chosen because it is a relevant density of small particles in the atmosphere (Kannosto et al., 2008). Only coagulation rates are affected by the density value.

3.1 Test cases

Artificial test cases were used to compare the PL+LN model output with a highly accurate FS model. The FS model had 1000 size sections between 1.6 and 10 nm and it is sufficiently dense to produce accurate results. Additionally, the PL+LN model was compared with the model having a log-normal distribution only (LN). All cases were simulated using constant and equal time steps to obtain a reliable comparison; the simulated times (t_max) were split into 3000 time steps.

The test cases are presented in Tab. 1. The Atm and Exh cases represent particle formation cases using input parameter values that reflect conditions typical to the atmosphere and to vehicle exhaust, respectively. Typical new particle formation rates in the atmosphere range from 0.01 to 10 $\mathrm{cm^{-3}s^{-1}}$ and condensational growth rates from 0.1 to 20 $\mathrm{nm/h}$ (Kulmala et al., 2004). In vehicle exhaust, new particle formation rates can reach up to $10^{10}\,\mathrm{cm^{-3}s^{-1}}$ and condensational growth rates up to $20\,\mathrm{nm/s}$ (Rönkkö et al., 2006; Uhrner et al., 2007; Olin et al., 2015). To test the PL+LN model in a wide range of J and g, low values for Atm cases ($J = 0.1\,\mathrm{cm^{-3}s^{-1}}$, $g = 1\,\mathrm{nm/h}$) and high values for the Exh case ($J = 10^8\,\mathrm{cm^{-3}s^{-1}}$, $g = 5\,\mathrm{nm/s}$) were chosen. Constant values for g denote time- and size-independent behavior for growth.

The Atm1 case includes simultaneous new particle formation, condensation, intramodal-, and intermodal coagulation. For the Atm2 case, depositional losses were also added. The deposition coefficient $k_{\mathrm{dep}} = 5\times10^{-4}\,\mathrm{nm/s}$ was calculated by assuming that particle formation takes place in a test chamber with the dimensions of $3\,\mathrm{m}\times2\,\mathrm{m}\times2\,\mathrm{m}$ and with the deposition velocities of salt particles measured by Hussein et al. (2009). For the Atm3 case, a background distribution was added to act as the coagulation sink. The chosen values for the number concentration $N_{\mathrm{bg}} = 10^3\,\mathrm{cm^{-3}}$ and count median diameter $\mathrm{CMD_{bg}} = 100\,\mathrm{nm}$ of the background distribution have been observed, e.g., in boreal forest area (Riipinen et al., 2007). The value for the coagulational loss exponent $l_{\mathrm{bg}} = -1.6$ was obtained from Lehtinen et al. (2007) using $\mathrm{CMD_{bg}} = 100\,\mathrm{nm}$. For Atm4 case, a bell-shaped time-dependent function for the new particle formation rate (a bell-shaped form in the function of the number concentration between 3 and 6 nm is seen in studies of Sihto et al. (2006); Riipinen et al. (2007)) was used:

$$J(t) = J_0\, e^{-\left(\frac{t-t_0}{\tau_{\mathrm{J}}}\right)^2}, \tag{53}$$

where $t_0 = 1000\,\mathrm{s}$ is the time at which the highest new particle formation rate $J_0 = 0.1\,\mathrm{cm^{-3}s^{-1}}$ occurs and $\tau_{\mathrm{J}} = 5000\,\mathrm{s}$ represents the width of the bell-shaped curve.

The Exh case represents simultaneous new particle formation, condensation, intramodal- and intermodal coagulation, coagulational losses, and depositional losses occurring in diesel vehicle exhaust inside the ageing chamber of a laboratory sampling system. The values $N_{\mathrm{bg}} = 10^6\,\mathrm{cm^{-3}}$ and $\mathrm{CMD_{bg}} = 60\,\mathrm{nm}$ were obtained from the measurements of Rönkkö et al. (2013) and the corresponding $l_{\mathrm{bg}} = -1.5$ from Lehtinen et al. (2007) using $\mathrm{CMD_{bg}} = 60\,\mathrm{nm}$. The deposition coefficient $k_{\mathrm{dep}} = 7\times10^{-2}\,\mathrm{nm/s}$ was calculated using the ageing chamber dimensions of 5 cm (diameter) × 100 cm (length) and the deposition velocities of salt particles measured by Hussein et al. (2009). The coagulational transfer was included in the simulations but the condensational transfer was not.

3.2 Mobile aerosol chamber particle formation event

A particle formation event performed in a mobile aerosol chamber was simulated using the PL+LN, LN, FS, and MC models. The output of the FS model with 720 size sections between 1.6 and 100 nm (FS720) was considered the most accurate number concentration result, and the output of the MC model with 100 size sections between 1.6 and 100 nm (MC100) the most accurate mass concentration result. Additionally, FS model with 24 size sections between 1.6 and 300 nm (FS24) and MC model with 6 size sections between 1.6 and 1000 nm (MC6) were used in comparing the computational cost and the accuracy of different models, because these section numbers provide nearly equal computing times as the PL+LN model. The upper limits for particle diameters of FS24 and MC6 models are higher due to their high numerical diffusion.

The mobile aerosol chamber is a Teflon bag with the dimensions of $3\,\mathrm{m}\times2\,\mathrm{m}\times2\,\mathrm{m}$. The chamber is operated in a batch process, i.e., firstly, the chamber is filled with the air sample, and secondly, the sample is measured from the chamber. UVC lights (254 nm) are used in the chamber to initiate new particle formation and to boost the aging of the aerosol through photochemical processes. The chamber simulates a particle formation event occurring in the atmosphere, but with shorter time scale due to the UV lights. The chamber is designed to be mobile; therefore, it is fit to a car trailer.

The particle formation event measurement was performed at street canyon measurement site of Helsinki Region Environmental Services Authority (HSY) located in Mäkelänkatu, Helsinki, Finland. The street had dense traffic during the measurement in April 22nd 2015. The chamber was firstly filled with urban air, and once filled; the air sample was sucked with the measurement devices located in the mobile laboratory vehicle. The aerosol sample was measured using Airmodus PSM, TSI Ultrafine Condensation Particle Counter (CPC), TSI Nano Scanning Mobility Particle Sizer (Nano-SMPS), TSI Engine Exhaust Particle Sizer (EEPS), and Dekati Electrical Low-Pressure Impactor (ELPI+). PSM in fixed saturator flow setting detects particles with the diameter from about 1.6 nm (Vanhanen et al., 2011), CPC from about 3.6 nm (Mordas et al., 2008), and Nano-SMPS from about 7 to 64 nm at the detection efficiency of 50 % or higher. These cut diameters are used to combine the data of PSM, CPC, and Nano-SMPS to obtain total aerosol size distributions for the diameter range of 1.6 – 64 nm. Nano-SMPS measures diameters down to 2 nm, but due to its low accuracy for those diameters, all Nano-SMPS data below 7 nm is neglected. EEPS and ELPI+ were used to ensure the stability of the aerosol distribution in shorter time scale.

Initially, the aerosol in the chamber consisted of a background aerosol mode with particle diameters around 15 nm and with the concentration of about 4000 cm^{-3}, according to the Nano-SMPS data shown in Fig. 4. No major changes in the distribution were observed until the UV lights were switched on. After switching on the UV lights, the number concentration and the particle diameters (Figs. 4 and 5) began to increase, i.e. the nucleation mode appeared. It can be also seen that small particles exist though the growth process proceeds, which implies continuing new particle formation. After about 500 s, particle concentration finished increasing, which occurs because all the gaseous precursors initiating new particle formation began to expire. The decreasing trend of particle number concentration after 500 s was accounted by coagulation and deposition. In the simulation of the event, a bell-shaped function as in Eq. (53) was used for the new particle formation rate, because it appeared to correspond well with the number concentration measured by PSM. In this case, the values $J_0 = 800\,\mathrm{cm}^{-3}\,\mathrm{s}^{-1}$, $t_0 = 368\,\mathrm{s}$, and $\tau_\mathrm{J} = 190\,\mathrm{s}$ were obtained from inverse modelling by comparing the number concentration of the model with the number concentration measured by PSM. The same shape was also used for the condensational growth rate function

$$g(t) = g_0\, e^{-\left(\frac{t-t_0}{\tau_\mathrm{g}}\right)^2}, \tag{54}$$

where $g_0 = 144\,\mathrm{nm/h}$, $t_0 = 418\,\mathrm{s}$, and $\tau_\mathrm{g} = 600\,\mathrm{s}$, which were obtained from inverse modelling by comparing the particle diameters of the model with the particle diameters measured by Nano-SMPS. Inverse modelling was performed, firstly, using a computationally efficient PL+LN model to obtain coarse estimates for $J(t)$ and $g(t)$, and lastly, using an accurate sectional model to fine tune the values. Inverse modelling was performed manually, i.e. iterating the input parameters $J(t)$ and $g(t)$ and checking the correspondence of the particle number concentration and the size distribution with the measured ones were done manually using a trial and error method.

Only the nucleation mode was simulated and the coagulational losses to the background mode were neglected. Depositional losses were modelled using the deposition coefficient $k_\mathrm{dep} = 0.01\,\mathrm{nm/s}$ which is obtained by fitting using the measured number concentration data after particle formation and growth were quenched ($t > 1500\,\mathrm{s}$). A time domain starting from 152 s before switching the UV lights on and ending to 1663 s after switching the UV lights on was simulated with 15000 equal time steps. During this time domain, particles are formed and grown to about $25\,\mathrm{nm}$, formation and condensational growth rates are changed, and the total distribution was altered from a power law-shape towards a log-normal-shape. Therefore, the simulation of this event provides a useful test to examine the performance of the PL+LN model in different shapes of a distribution and in changing real-world case.

The distributions measured in the chamber were relatively wide, GSD values in the Nano-SMPS data were up to 1.8. For that reason, the condensational transfer was used in the PL+LN model to provide wide LN distributions; the value of γ was set to 0.8 providing the best corresponding shapes of the distribution compared to the measured ones. Due to high γ, the coagulational transfer would have had a minor effect only; thus, it was neglected from the simulation. The factor γ is a free parameter having no explicit physical meaning; thus, the sensitivity of the value of γ was also examined using additionally the values 0.1, 0.5, and 0.9 for it.

4 Results and discussion

4.1 Test cases

Figure 6 shows the size distributions at the ends of the test simulations using different models. It can be observed from those that the shape of the distribution produced by the PL+LN model is nearly equal as the reference distribution (FS1000). The largest deviations between the PL+LN distributions and the reference distributions are the gap between the PL and the LN distribution and the sharp peak in the PL distribution. These are most clearly seen in the Atm4 case where α is highest. Conversely, the distributions produced by the LN model are far beyond the reference distributions. In the Atm4 case where new particle formation rate decreases towards the end of the simulation, the LN model begins to act better while the reference distribution transforms towards a log-normal shape.

The effect of the depositional losses can be seen as a decreased α in the Atm2 case compared to the Atm1 case. Because $k_{\mathrm{dep}} > g$, the value of α becomes negative. Comparing the Atm3 case with the Atm2 case, it can be seen that the coagulational losses decrease α further. Using a decreasing function for $J(t)$ but time-independent g as in the Atm4 case, α increases again, because there will be less small particles with increasing time. The distribution of the Exh case is mainly comparable to the Atm1 case with the exception of higher concentrations in the Exh case due to higher $\frac{J}{g}$. It can be also observed that the ratio of the concentrations of the LN distribution and of the PL distribution is higher in the Exh case than in the Atm1 case. This is due to increased coagulational transfer in the Exh case because it is calculated through the intramodal coagulation, which is proportional to N_{PL}^2.

Table 2 shows the relative errors of the variables in the PL+LN model compared to the reference model (FS1000) at the ends of the test simulations. The relative errors of the total concentrations N, S, and M are less than $2\,\%$ in all the cases, total number concentration N being the most accurate. GMD and GSD have the relative errors of less than 0.5 % in the cases with time-independent parameters, but for the Atm4 case the errors are higher (around $\pm 2\,\%$) due to time-dependent new particle formation rate.

4.2 Mobile aerosol chamber particle formation event

Particle size distributions obtained from the FS720, LN, and PL+LN models are shown as contour plots in Fig. 4 together with the measured distributions. Comparing the plots of the LN and PL+LN models with the plot of the FS720 model, it can be seen that the PL+LN model behaves better for small diameters than the LN model. However, there is a sharp discontinuity between the PL and the LN distributions in the PL+LN model. In this case, the discontinuity is mainly formed due to the condensational transfer that is separating the distributions from each other. It is also seen that the PL+LN model is capable in vanishing the PL distribution when the aerosol ages and begins to have mainly a log-normal form. Particle distributions 528 s after the UV lights switched on are also shown in Fig. 7. The shape of the distribution produced by the PL+LN model is near the reference distribution (FS720) with the exception of the gap between the PL and the LN distribution. The shape of the distribution at the largest particles produced by the LN model corresponds better with the measured distribution than at the smallest particles. In the simulation using the FS24 model, a high numerical diffusion that widens the distribution towards the larger particles is seen.

Table 3 represents the computational costs and the accuracies of the models. Computational costs are reported as computing times relative to the computing time of the PL+LN simulation (110 s). All simulations were run using the same computer (Intel Core i5-3470 processor at 3.2 GHz). The PL+LN model has the best accuracy for the total number (N) and mass (M) concentrations compared to the sectional models with approximately the same computing time (FS24 and MC6) and to the LN model. The FS24 model, however, is more accurate in N output but suffers from high numerical diffusion seen as high relative error ($135\,\%$) in M. The PL+LN model has also low memory consumption due to a low number of variables. The LN model has, however, the most computational efficiency but the relative errors are high too (up to $9.87\,\%$ in N).

The development of N is shown in Fig. 5, from which it can be seen that the PL+LN model has nearly the same output for N as the reference models during the whole time domain. The beginning of the overestimation of N in the LN and in the MC6 models are clearly seen at the region where the new particle formation has the highest rate ($t_0 = 368\,\mathrm{s}$). The development of GMD can be seen from Fig. 8: the PL+LN model produces GMD accurately during the whole time domain, the LN model nearly as accurately as the PL+LN model, but the FS24 model overestimates GMD at the end of the simulation due to numerical diffusion. The MC6 model overestimates GMD during the whole time domain and has uneven features. The highest deviations between the models are seen in the development of GSD (Fig. 9). The PL+LN model underestimates GSD slightly at the end of the time domain, the LN model significantly at the time of the highest new particle formation rates and slightly at the end of the time domain. The FS24 model overestimates GSD significantly during the whole time domain and the MC6 model suffers from uneven behavior and underestimations. The development of GMD and GSD for the measurement data is not shown due to the lack of an accurate distribution data for the diameters below the Nano-SMPS measurement range. In conclusion, the PL+LN model has the best accuracy for the production of N, GMD, and GSD during the whole time domain compared to the other models having at least the same computational efficiency (LN, FS24, and MC6).

The functions $J(t)$ and $g(t)$ can be optimized so that the other models would produce the most accurate time series for N, GMD, and GSD if the comparison is done against the measurement data. E.g., the LN model would produce an accurate time series for N if $J(t)$ is decreased approximately with $10\,\%$. However, in that kind of inverse modelling, too low $J(t)$ is obtained because the most correct $J(t)$ would be obtained from the most accurate model, a sectional model. Therefore, the comparison must be done against the output of a sectional model rather than the measurement data. Additionally, an incorrectly predicted $J(t)$ would also cause errors in the prediction of other parameters, such as $g(t)$.

Figure 10 represents the same distributions as in Fig. 7, but with the PL+LN model using different values for γ. It can be seen that the PL distribution in the total distribution is mostly dominating when a low value for γ is used. Conversely, a high value produces more a log-normal like form, which, at least in this case, corresponds best with the measured distribution. However, a gap between the PL and the LN distributions is larger in cases of high values of γ. The sensitivity of the value of γ is also shown in Tab. 4, in which the relative errors of N, M, GMD, and GSD are reported. It can be seen that a value between 0.5 and 0.8 may provide the most accurate results, depending on the variable of the main interest. Comparing the errors of N and M produced by the PL+LN model with the errors produced by different models reported in Tab. 3, it can be seen that the lowest errors for N and M simultaneously are produced by the PL+LN model regardless of the value of γ used.

5 Conclusions

The combined power law and log-normal distribution (PL+LN) model was developed to represent a particle size distribution in simultaneous new particle formation and growth situation, in which log-normal distributions do not represent the aerosol sufficiently well. The PL+LN distribution combines a power law form typical to simultaneous new particle formation and growth situation at the initial steps of aerosol formation with a log-normal form typical to aged aerosols. The PL+LN model is useful in simulations involving the initial steps of aerosol formation where a sectional representation of the size distribution causes too high computational cost, such as in multidimensional simulations or in the case of obtaining input parameters as the model output through inverse modelling. These parameters can be, e.g., new particle formation rate or the condensational growth rate that most accurately produce the distributions as the measured ones. The model uses six moment variables to model the distribution, denoting lower memory consumption compared to sectional models which require tens or hundreds variables. The model includes simultaneous new particle formation, condensation, coagulation, coagulational loss, and depositional loss processes.

The PL+LN model was validated and tested using test simulations and a real-world particle formation event simulation. The test cases represented particle formation events with the parameters related to the atmosphere and to vehicle exhaust. The real-world case was the simulation of a particle formation event measurement performed in a mobile aerosol chamber at Mäkelänkatu street canyon measurement site in Helsinki, Finland. The validation was done against highly accurate sectional models using fixed-sectional and moving-center fixed-sectional methods. The conservation of the total number, surface area, and mass concentrations in the PL+LN model was examined: the relative errors of the concentrations were lower than $2\,\%$ compared to the highly accurate sectional models. The performance of producing geometric mean diameter (GMD) and geometric standard deviation (GSD) of the total distributions in the test cases using different models was also examined: the highest relative error with the PL+LN model was 2.143 % for GSD when time-dependent new particle formation rate was modelled, but the errors were lower than 0.5 % when constant rate was modelled. The shapes of the distributions produced by the PL+LN model were noticeably more similar to the reference distributions than produced by a simple log-normal distribution model.

Considering the same computing time as the PL+LN model in the chamber event simulation, only 24 size sections for fixed-sectional and 6 size sections for moving-center fixed-sectional models were allowed to be modelled. With these section numbers, the results for the number and mass concentrations, for GMD, and for GSD were not as accurate as using the PL+LN model. Additionally, simple log-normal distribution model output GMD relatively well but overestimated number concentration and underestimated GSD.

Acknowledgements. This work was funded by the Maj and Tor Nessling Foundation (project number 2014452), by Tampere University of Technology Graduate School, and by the Finnish Funding Agency for Technology and Innovation (Tekes) as a part of the CLEEN MMEA program. Authors acknowledge the personal of the Air Protection Group at the Helsinki Region Environmental Services Authority (HSY) for enabling the measurement campaign at the HSY's street canyon measurement site in Helsinki.

References

Barrett, J. and Webb, N.: A comparison of some approximate methods for solving the aerosol general dynamic equation, J. Aerosol Sci., 29, 31–39, doi:10.1016/S0021-8502(97)00455-2, 1998.

Dahneke, B.: Simple kinetic theory of Brownian diffusion in vapors and aerosols, in: Theory of Dispersed Multiphase Flow, edited by Meyer, R. E., pp. 97–133, Academic Press, doi:10.1016/B978-0-12-493120-6.50011-8, 1983.

Hinds, W. C.: Aerosol technology: properties, behavior, and measurement of airborne particles, John Wiley & Sons, Inc., Hoboken, USA, 2nd edn., 1999.

Hussein, T., Hruška, A., Dohányosová, P., Džumbová, L., Hemerka, J., Kulmala, M., and Smolík, J.: Deposition rates on smooth surfaces and coagulation of aerosol particles inside a test chamber, Atmos. Environ., 43, 905–914, doi:10.1016/j.atmosenv.2008.10.059, 2009.

Jacobson, M.: Development and application of a new air pollution modeling system–II. Aerosol module structure and design, Atmos. Environ., 31, 131–144, doi:10.1016/1352-2310(96)00202-6, 1997.

Kannosto, J., Virtanen, A., Lemmetty, M., Mäkelä, J. M., Keskinen, J., Junninen, H., Hussein, T., Aalto, P., and Kulmala, M.: Mode resolved density of atmospheric aerosol particles, Atmos. Chem. Phys., 8, 5327–5337, doi:10.5194/acp-8-5327-2008, 2008.

Kerminen, V.-M. and Kulmala, M.: Analytical formulae connecting the "real" and the "apparent" nucleation rate and the nuclei number concentration for atmospheric nucleation events, J. Aerosol Sci., 33, 609–622, doi:10.1016/S0021-8502(01)00194-X, 2002.

Kulmala, M., Vehkamäki, H., Petäjä, T., Maso, M. D., Lauri, A., Kerminen, V.-M., Birmili, W., and McMurry, P.: Formation and growth rates of ultrafine atmospheric particles: a review of observations, J. Aerosol Sci., 35, 143–176, doi:10.1016/j.jaerosci.2003.10.003, 2004.

Kulmala, M., Riipinen, I., Sipilä, M., Manninen, H. E., Petäjä, T., Junninen, H., Dal Maso, M., Mordas, G., Mirme, A., Vana, M., Hirsikko, A., Laakso, L., Harrison, R. M., Hanson, I., Leung, C., Lehtinen, K. E. J., and Kerminen, V.-M.: Toward direct measurement of atmospheric nucleation, Science, 318, 89–92, doi:10.1126/science.1144124, 2007.

Kulmala, M., Kontkanen, J., Junninen, H., Lehtipalo, K., Manninen, H., Nieminen, T., Petäjä, T., Sipilä, M., Schobesberger, S., Rantala, P., Franchin, A., Jokinen, T., Järvinen, E., Äijälä, M., Kangasluoma, J., Hakala, J., Aalto, P., Paasonen, P., Mikkilä, J., Vanhanen, J., Aalto, J., Hakola, H., Makkonen, U., Ruuskanen, T., Mauldin III, R., Duplissy, J., Vehkamäki, H., Bäck, J., Kortelainen, A., Riipinen, I., Kurtén, T., Johnston, M., Smith, J., Ehn, M., Mentel, T., Lehtinen, K., Laaksonen, A., Kerminen, V.-M., and Worsnop, D.: Direct observations of atmospheric aerosol nucleation, Science, 339, 943–946, doi:10.1126/science.1227385, 2013.

Lai, A. and Nazaroff, W.: Modeling indoor particle deposition from turbulent flow onto smooth surfaces, J. Aerosol Sci., 31, 463–476, doi:10.1016/S0021-8502(99)00536-4, 2000.

Lehtinen, K. E. J. and Kulmala, M.: A model for particle formation and growth in the atmosphere with molecular resolution in size, Atmos. Chem. Phys., 3, 251–257, doi:10.5194/acp-3-251-2003, 2003.

Lehtinen, K. E. J., Dal Maso, M., Kulmala, M., and Kerminen, V.-M.: Estimating nucleation rates from apparent particle formation rates and vice versa: Revised formulation of the Kerminen-Kulmala equation, J. Aerosol Sci., 38, 988–994, doi:10.1016/j.jaerosci.2007.06.009, 2007.

McGraw, R.: Description of aerosol dynamics by the quadrature method of moments, Aerosol Sci. Tech., 27, 255–265, doi:10.1080/02786829708965471, 1997.

Mitrakos, D., Hinis, E., and Housiadas, C.: Sectional modeling of aerosol dynamics in multi-dimensional flows, Aerosol Sci. Tech., 41, 1076–1088, doi:10.1080/02786820701697804, 2007.

Mordas, G., Manninen, H., Petäjä, T., Aalto, P., Hämeri, K., and Kulmala, M.: On operation of the ultra-fine water-based CPC TSI 3786 and comparison with other TSI models (TSI 3776, TSI 3772, TSI 3025, TSI 3010, TSI 3007), Aerosol Sci. Tech., 42, 152–158, doi:10.1080/02786820701846252, 2008.

Olin, M., Rönkkö, T., and Dal Maso, M.: CFD modeling of a vehicle exhaust laboratory sampling system: sulfur-driven nucleation and growth in diluting diesel exhaust, Atmos. Chem. Phys., 15, 5305–5323, doi:10.5194/acp-15-5305-2015, 2015.

Riipinen, I., Sihto, S.-L., Kulmala, M., Arnold, F., Dal Maso, M., Birmili, W., Saarnio, K., Teinilä, K., Kerminen, V.-M., Laaksonen, A., and Lehtinen, K. E. J.: Connections between atmospheric sulphuric acid and new particle formation during QUEST III–IV campaigns in Heidelberg and Hyytiälä, Atmos. Chem. Phys., 7, 1899–1914, doi:10.5194/acp-7-1899-2007, 2007.

Rönkkö, T., Virtanen, A., Vaaraslahti, K., Keskinen, J., Pirjola, L., and Lappi, M.: Effect of dilution conditions and driving parameters on nucleation mode particles in diesel exhaust: Laboratory and on-road study, Atmos. Environ., 40, 2893–2901, doi:10.1016/j.atmosenv.2006.01.002, 2006.

Rönkkö, T., Lähde, T., Heikkilä, J., Pirjola, L., Bauschke, U., Arnold, F., Schlager, H., Rothe, D., Yli-Ojanperä, J., and Keskinen, J.: Effects of gaseous sulphuric acid on diesel exhaust nanoparticle formation and characteristics, Environ. Sci. Technol., 47, 11 882–11 889, doi:10.1021/es402354y, 2013.

Seinfeld, J. and Pandis, S.: Atmospheric Chemistry and Physics: From Air Pollution to Climate Change, John Wiley and Sons, Inc., New York, USA, 2nd edn., 2006.

Sihto, S.-L., Kulmala, M., Kerminen, V.-M., Dal Maso, M., Petäjä, T., Riipinen, I., Korhonen, H., Arnold, F., Janson, R., Boy, M., Laaksonen, A., and Lehtinen, K. E. J.: Atmospheric sulphuric acid and aerosol formation: implications from atmospheric measurements for nucleation and early growth mechanisms, Atmos. Chem. Phys., 6, 4079–4091, doi:10.5194/acp-6-4079-2006, 2006.

Steen, N., Byrne, G., and Gelbard, E.: Gaussian quadratures for the integrals $\int_0^\infty \exp(-x^2)f(x)dx$ and $\int_0^b \exp(-x^2)f(x)dx$, Math. Comp., 23, 661–671, 1969.

Tammet, H. and Kulmala, M.: Performance of four-parameter analytical models of atmospheric aerosol particle size distribution, J. Aerosol Sci., 77, 145 – 157, doi:10.1016/j.jaerosci.2014.08.001, 2014.

Uhrner, U., von Löwis, S., Vehkamäki, H., Wehner, B., Bräsel, S., Hermann, M., Stratmann, F., Kulmala, M., and Wiedensohler, A.: Dilution and aerosol dynamics within a diesel car exhaust plume-CFD simulations of on-road measurement conditions, Atmos. Environ., 41, 7440–7461, doi:10.1016/j.atmosenv.2007.05.057, 2007.

Vanhanen, J., Mikkilä, J., Lehtipalo, K., Sipilä, M., Manninen, H. E., Siivola, E., Petäjä, T., and Kulmala, M.: Particle size magnifier for nano-CN detection, Aerosol Sci. Tech., 45, 533–542, doi:10.1080/02786826.2010.547889, 2011.

Verheggen, B. and Mozurkewich, M.: An inverse modeling procedure to determine particle growth and nucleation rates from measured aerosol size distributions, Atmos. Chem. Phys., 6, 2927–2942, doi:10.5194/acp-6-2927-2006, 2006.

Wang, Y. and Zhang, K.: Coupled turbulence and aerosol dynamics modeling of vehicle exhaust plumes using the CTAG model, Atmos. Environ., 59, 284–293, doi:10.1016/j.atmosenv.2012.04.062, 2012.

Whitby, E. and McMurry, P.: Modal aerosol dynamics modeling, Aerosol Sci. Tech., 27, 673–688, doi:10.1080/02786829708965504, 1997.

Wu, C.-Y. and Biswas, P.: Study of numerical diffusion in a discrete-sectional model and its application to aerosol dynamics simulation, Aerosol Sci. Tech., 29, 359–378, doi:10.1080/02786829808965576, 1998.

Atmos. Chem. Phys. Discuss., doi:10.5194/acp-2015-1007, 2016
Manuscript under review for journal Atmos. Chem. Phys.
Published: 19 January 2016

Table 1. Input parameters for the test cases. Case names with Atm have the parameter sets related to atmospheric particle formation and the Exh case related to particle formation occurred in vehicle exhaust. J and $g(t)$ are new particle formation rate and condensational growth rate, respectively. N_{bg} is the concentration of the background aerosol distribution having a count median diameter of $\mathrm{CMD}_{\mathrm{bg}}$. The coagulational loss exponent l_{bg} depend on the value of $\mathrm{CMD}_{\mathrm{bg}}$. Wall deposition is modelled using the deposition coefficient k_{dep}. The simulated time is t_{max}.

Case	J $(\mathrm{cm}^{-3}\mathrm{s}^{-1})$	$g(t)$	T (K)	Coagulation	N_{bg} (cm^{-3})	$\mathrm{CMD}_{\mathrm{bg}}$ (nm)	l_{bg}	k_{dep}	t_{max}
Atm1	0.1	1 nm/h	280	intra, inter	0	–	–	0	5 h
Atm2	0.1	1 nm/h	280	intra, inter	0	–	–	1.8 nm/h	5 h
Atm3	0.1	1 nm/h	280	intra, inter, bg	10^3	100	-1.6	1.8 nm/h	5 h
Atm4	Eq. (53)	1 nm/h	280	intra, inter, bg	10^3	100	-1.6	1.8 nm/h	5 h
Exh	10^8	5 nm/s	500	intra, inter, bg	10^6	60	-1.5	0.07 nm/s	1 s

Table 2. Relative errors (%) of the variables in the test cases using the PL+LN model compared to the variables produced by the fixed-sectional model with 1000 size sections. The input parameter sets are shown in Tab. 1. N, S, and M are the number, the surface area, and the mass concentration of the total particle distribution, respectively. GMD and GSD are the geometric mean diameter and the geometric standard deviation of the distribution.

Case	N	S	M	GMD	GSD
Atm1	-0.001	-0.312	-0.574	+0.067	-0.195
Atm2	-0.056	-0.482	-0.838	-0.080	-0.036
Atm3	+0.182	-0.868	-1.286	-0.085	-0.497
Atm4	+0.037	-0.845	-1.526	+1.716	-2.143
Exh	-0.347	-0.705	-0.982	+0.011	-0.213

Table 3. Computational costs and relative errors of different models using the chamber data. The number of variables compared to size sections in MC models is twofold because the centers of the size sections need to be stored in addition to the concentration in the sections. Relative numbers are calculated using a model with (ref.) as the reference model. Number (N) and mass (M) concentrations are obtained from the time of 1663 s after the UV lights switched on.

Model name	Method	Size sections	Variables	Relative computing time	Error in N (%)	Error in M (%)
FS24	fixed-sectional	24	24	1.0	+0.78	+135
MC6	moving-center	6	12	1.6	+26.4	+59.0
LN	log-normal	-	3	0.11	+9.87	+7.40
PL+LN	combined PL and LN	-	6	1 (ref.)	+1.14	-0.34
FS720	fixed-sectional	720	720	2000	0 (ref.)	+1.63
MC100	moving-center	100	200	100	+0.28	0 (ref.)

Table 4. Relative errors (%) of the variables in the chamber simulation with the PL+LN model using different values for the condensational transfer factor γ. The errors are compared to the FS720 model, except for M that is compared to the MC100 model.

γ	N	M	GMD	GSD
0.1	-5.64	-5.81	+4.40	-3.38
0.5	-1.09	-1.75	-0.53	-0.06
0.8	+1.14	-0.34	+1.00	-2.37
0.9	+3.03	+1.26	-0.22	-2.65

Atmos. Chem. Phys. Discuss., doi:10.5194/acp-2015-1007, 2016
Manuscript under review for journal Atmos. Chem. Phys.
Published: 19 January 2016

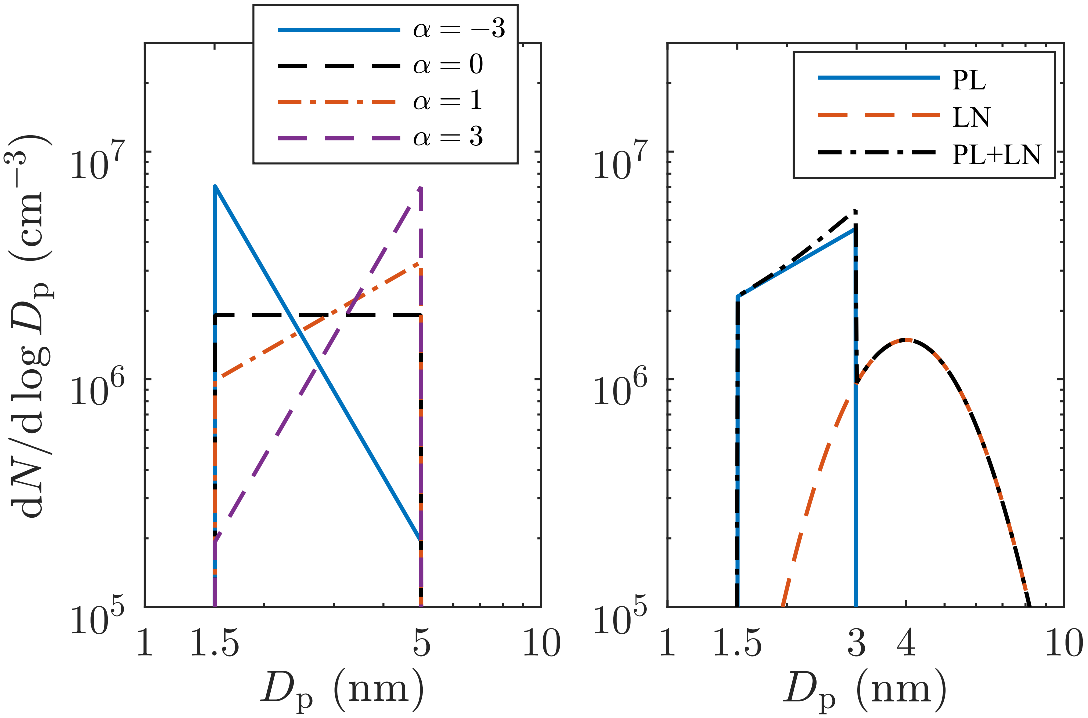

Figure 1. Left pane shows examples of power law distributions with different values of the slope parameter α. Right pane shows the combination of a power law (PL) and a log-normal (LN) distribution (PL+LN).

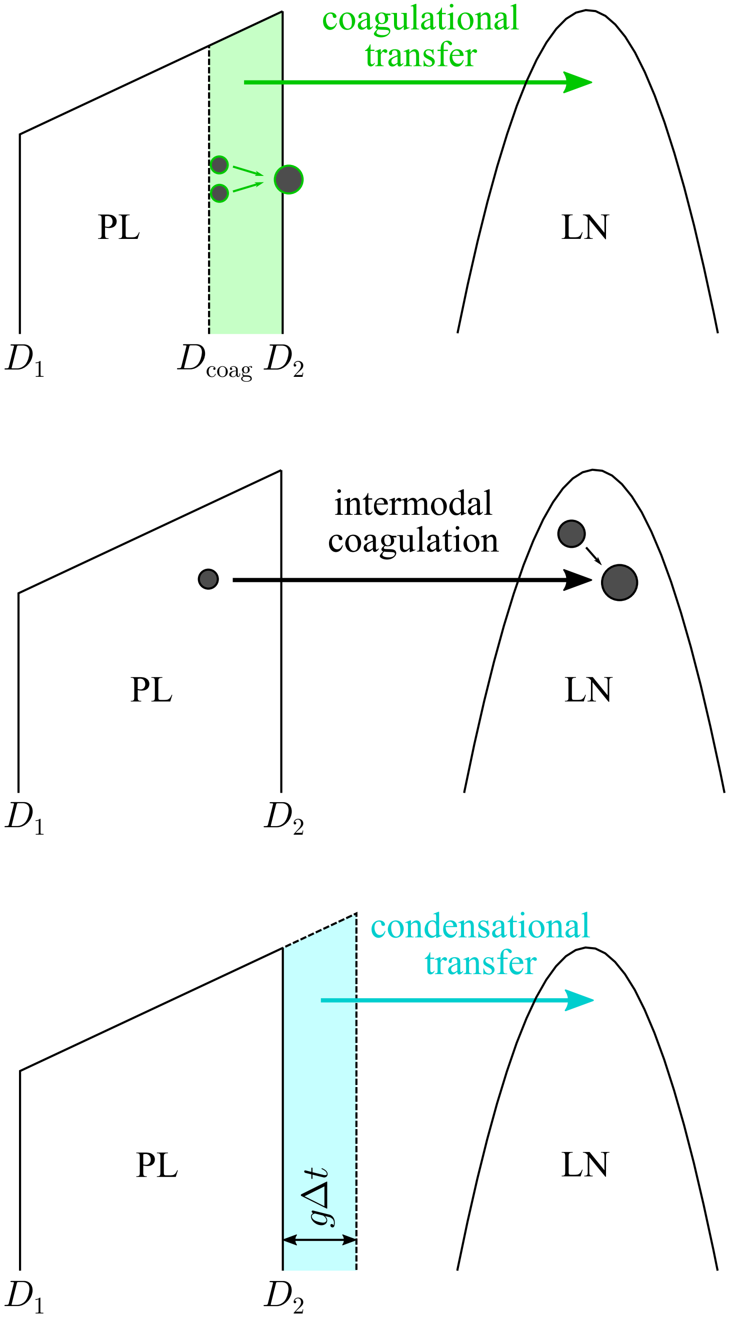

Figure 2. Intermodal processes between the PL and the LN distributions. Particles larger than D_{coag} (green area) form particles larger than D_2 by the intramodal coagulation in the PL distribution; the coalesced resultant particles are transferred to the LN distribution. When the LN distribution exists, particles of the both distributions begin to coagulate intermodally; the resultant particles are assigned to the LN distribution. Condensation grows the largest particle diameter by $g\Delta t$ in a time step of Δt, but the condensational transfer transfers a part of the particles larger than D_2 (blue area) to the LN distribution.

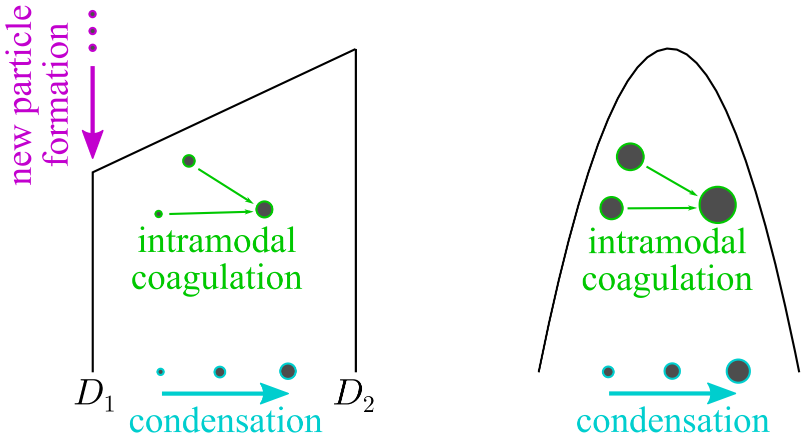

Figure 3. Intramodal processes. New particle formation forms particles with the diameter of D_1 to the PL distribution. Condensation and intramodal coagulation grow particles within a distribution.

Atmos. Chem. Phys. Discuss., doi:10.5194/acp-2015-1007, 2016
Manuscript under review for journal Atmos. Chem. Phys.
Published: 19 January 2016

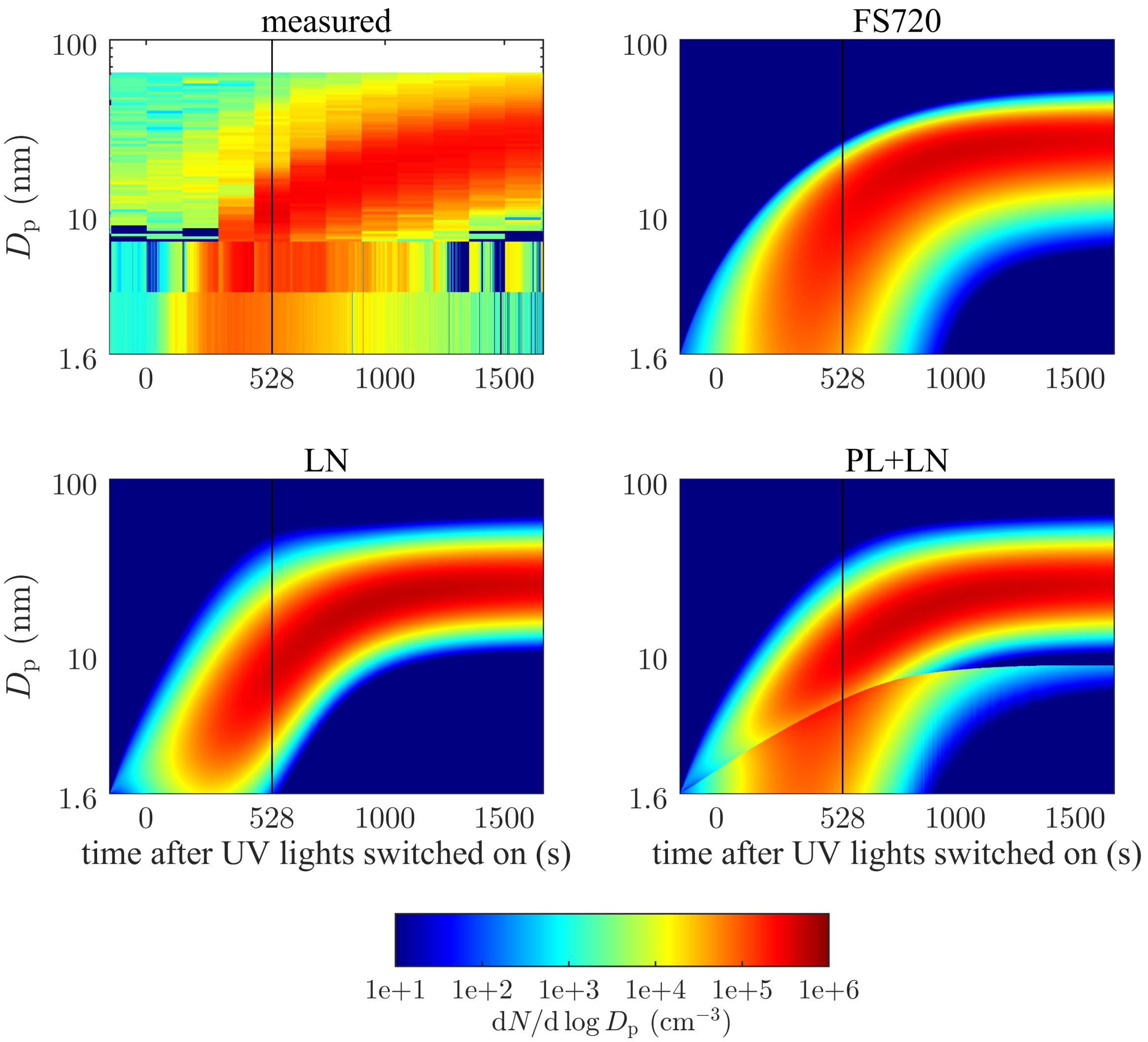

Figure 4. Contour plots of particle distributions measured by PSM, CPC, and Nano-SMPS and simulated by different models. FS720 denotes the fixed-sectional model with 720 size sections. Note that the background particle distribution seen in the measured data was excluded from the simulations. The vertical lines at 528 s indicate the time of the center of a Nano-SMPS scan for which the distributions are plotted also in Fig. 7.

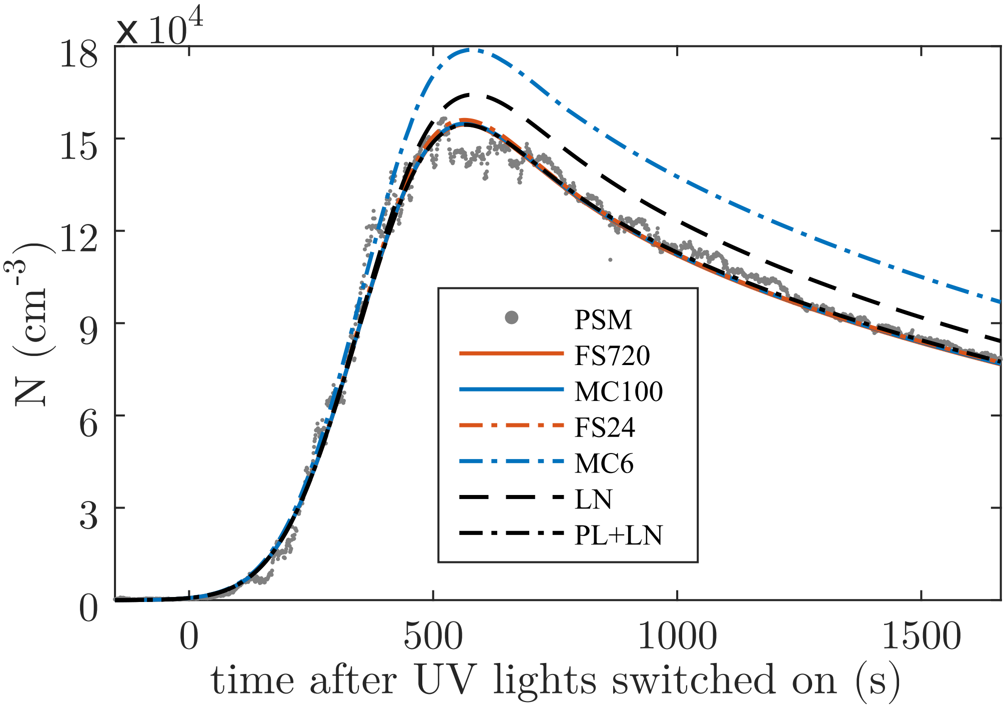

Figure 5. The development of the nucleation mode particle number concentration in the chamber event. PSM dots denote the measured concentration (subtracted by the background aerosol concentration) and the others the simulated concentrations. Concentrations from all the models except MC6 and LN are nearly equal at the end of the simulations. The abbreviations are explained in Tab. 3.

Atmos. Chem. Phys. Discuss., doi:10.5194/acp-2015-1007, 2016
Manuscript under review for journal Atmos. Chem. Phys.
Published: 19 January 2016

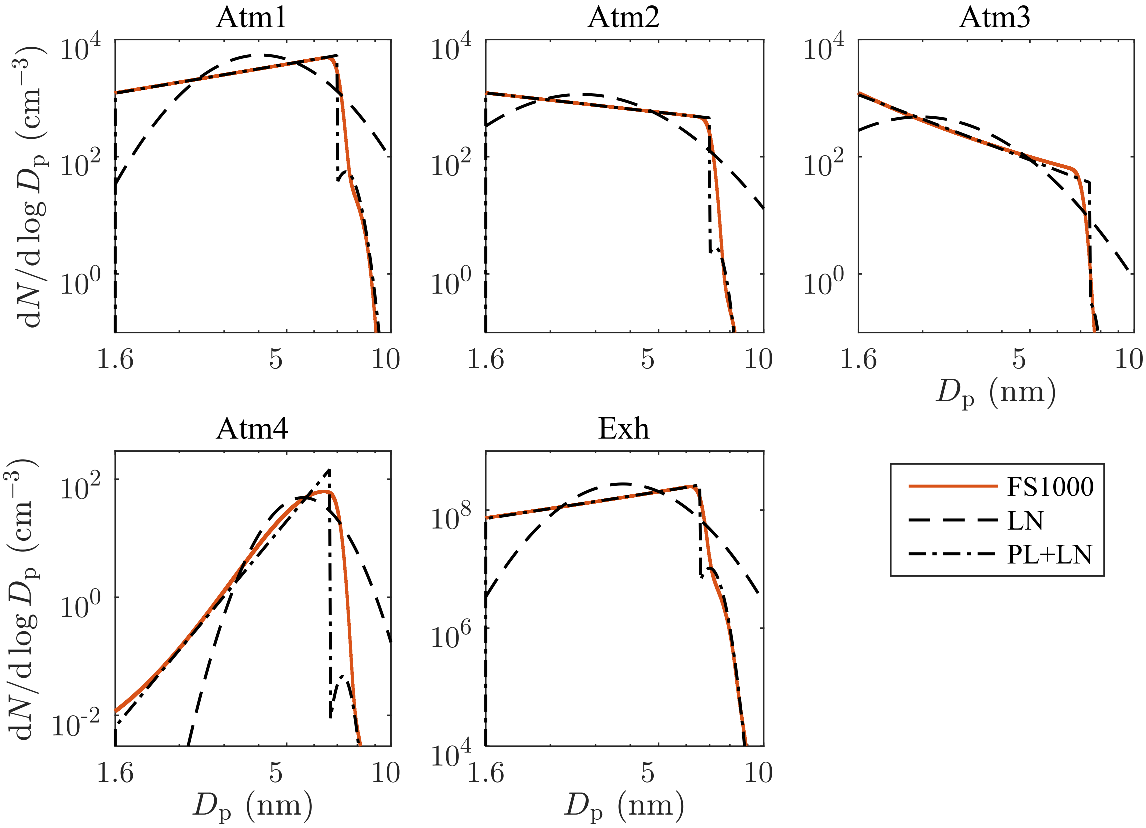

Figure 6. The size distributions of the test cases produced by different models. The input parameter sets are shown in Tab. 1. FS1000 denotes the fixed-sectional model with 1000 size sections. Note the different scales in the vertical axes on the bottom row.

Atmos. Chem. Phys. Discuss., doi:10.5194/acp-2015-1007, 2016
Manuscript under review for journal Atmos. Chem. Phys.
Published: 19 January 2016

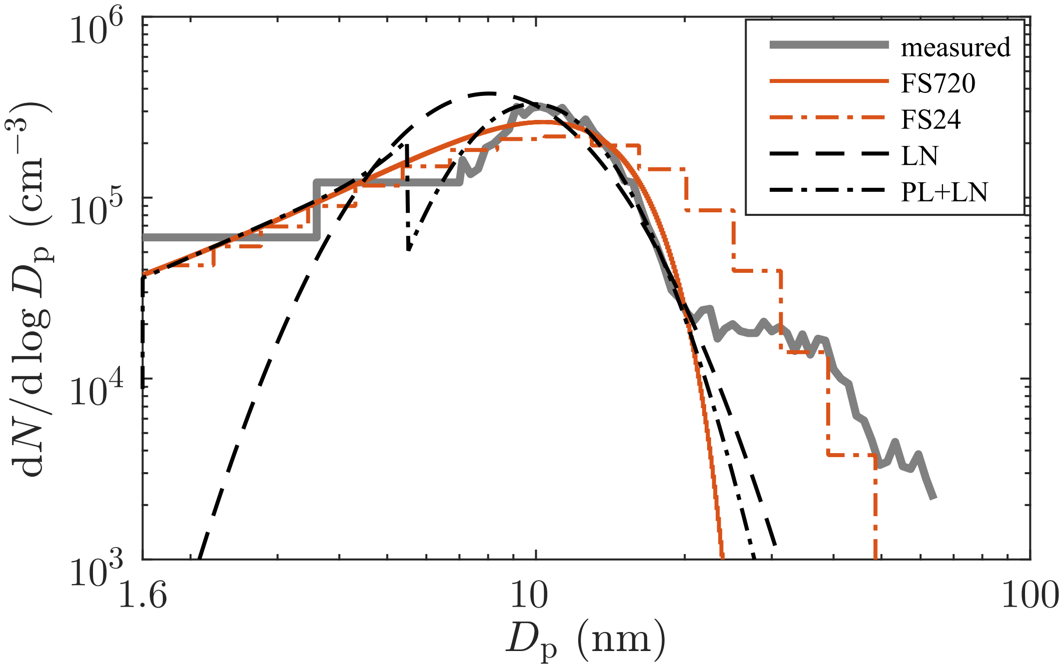

Figure 7. Particle size distributions in the chamber event 528 s after the UV lights switched on. The measured distribution includes also the background mode around 30 nm which was excluded from the simulations. The abbreviations are explained in Tab. 3.

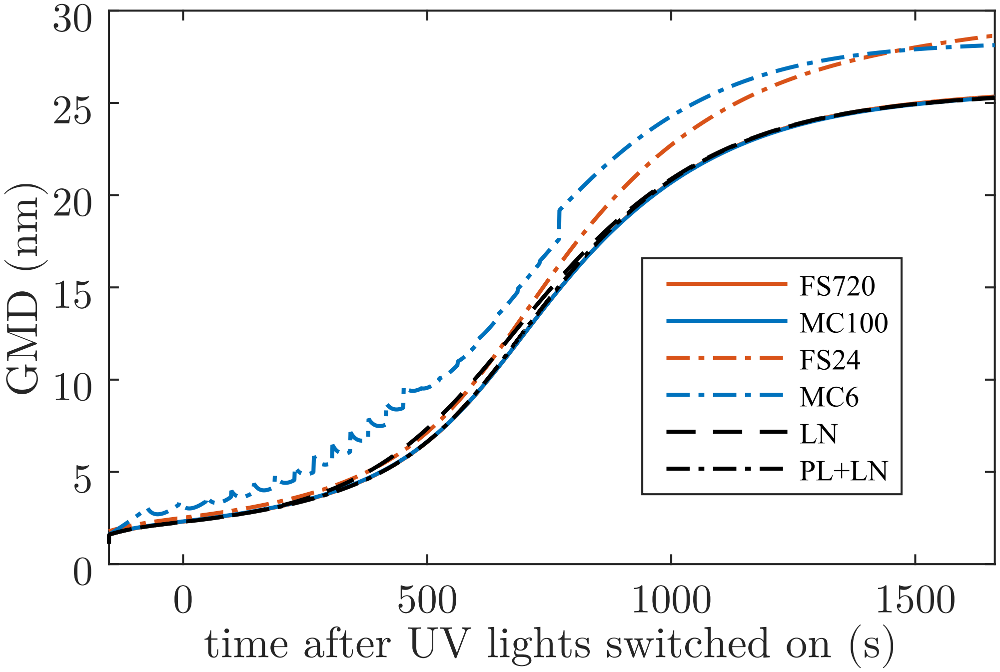

Figure 8. The development of the nucleation mode geometric mean diameter in the chamber event simulation. The values from all the models except FS24 and MC6 are nearly equal at the end of the simulations. The abbreviations are explained in Tab. 3.

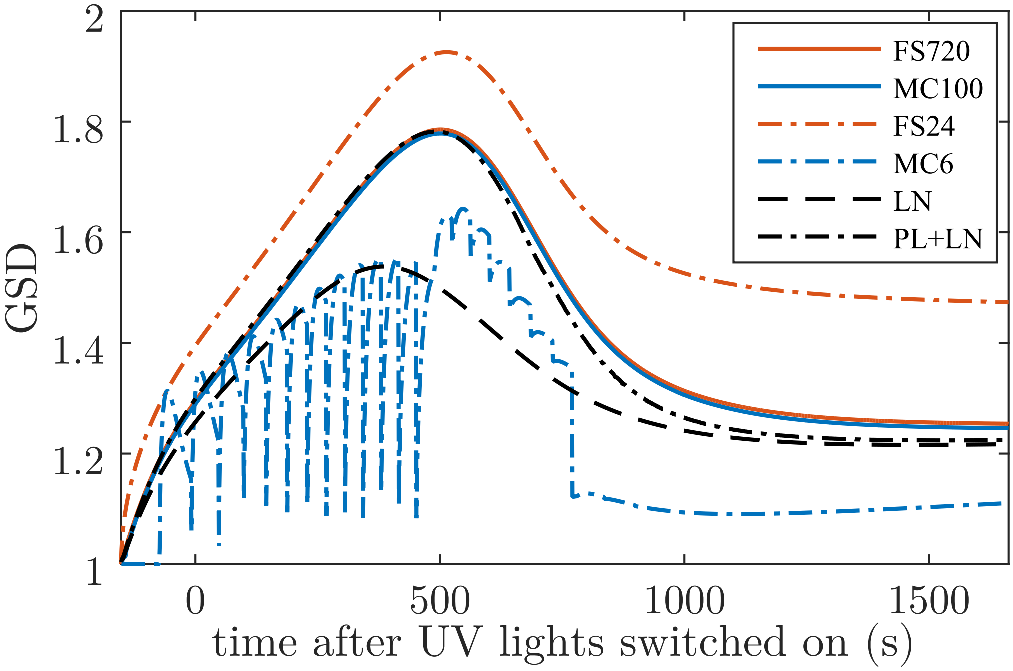

Figure 9. The development of the nucleation mode geometric standard deviation in the chamber event simulation. The abbreviations are explained in Tab. 3.

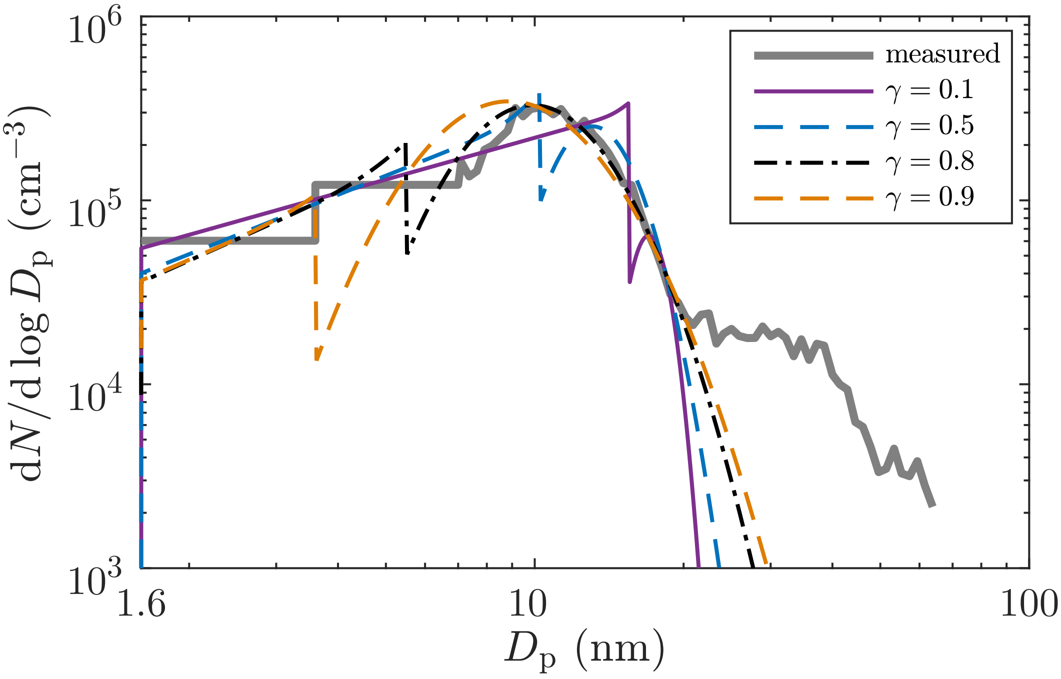

Figure 10. Particle size distributions as in Fig. 7, but with the different values for the condensational transfer factor γ using the PL+LN model.